RNA-programmable cell type monitoring and manipulation in the human cortex with CellREADR

Elizabeth A. Matthews[1,2], Jeffrey B. Russ[1,3], Yongjun Qian[2,5], Shengli Zhao[2], Peyton Thompson[1,2], Muhib Methani[1,2], Matthew L. Vestal[1,6], Z. Josh Huang[2,4 **], Derek G. Southwell[1,2,4 *]

Affiliations:

1. Department of Neurosurgery, Duke University School of Medicine, Durham, NC USA
2. Department of Neurobiology, Duke University School of Medicine, Durham, NC USA
3. Department of Pediatrics, Division of Neurology, Duke University School of Medicine, Durham, NC USA
4. Department of Biomedical Engineering, Duke University Pratt School of Engineering, Durham, NC USA
5. Current affiliation: College of Future technology, Peking-Tsinghua Center for Life Sciences, IDG/McGovern Institute for Brain Research, Beijing Advanced Center of RNA Biology (BEACON), Peking University, China
6. Current affiliation: Department of Neurosurgery, Dartmouth University, Dartmouth, MA USA

Corresponding authors:
* Derek G. Southwell (derek.southwell@duke.edu)
** Z. Josh Huang (josh.huang@duke.edu)

Abstract

Reliable and systematic experimental access to diverse cell types is necessary for understanding the neural circuit organization, function, and pathophysiology of the human brain. Methods for targeting human neural populations are scarce and currently center around identifying and engineering transcriptional enhancers and viral capsids. Here we demonstrate the utility of CellREADR, a programmable RNA sensor-effector technology that couples cellular RNA sensing to effector protein translation, for accessing, monitoring, and manipulating specific neuron types in *ex vivo* human cortical tissues. We designed CellREADR constructs to target two distinct human neuron types, *CALB2*+ (calretinin) GABAergic interneurons and *FOXP2*+ (forkhead box protein P2) glutamatergic projection neurons, and validated cell targeting using histological, electrophysiological, and transcriptomic methods. CellREADR-mediated expression of optogenetic effectors and genetically-encoded calcium indicators allowed us to manipulate and monitor these neuronal populations in cortical microcircuits. We further demonstrate that AAV-based CellREADR and enhancer vectors can be jointly used to target different subpopulations in the same preparation. By demonstrating specific, reliable, and programmable experimental access to targeted cell types, our results highlight CellREADR's potential for studying human neural circuits and treating brain disorders with cell type resolution.

Introduction

The human brain has evolved divergent and species-specific properties that underlie our unique cognitive and behavioral capabilities. While approaches such as MRI, EEG, and post-mortem neuroanatomical studies have identified some of the brain areas, functional networks, and fiber tracts involved in human sensorimotor, cognitive, and emotional functions and their related disorders, brain function fundamentally emerges from neural circuit computations performed by diverse, synaptically interacting cell populations. To better understand the neural underpinnings of human behaviors and neurological conditions, it is thus essential to investigate the fundamental elements of the brain - the diverse human neural cell types - and to dissect their functional features and dynamic interactions at the spatiotemporal resolution of neural circuit operation[1,2]. This requires 1) identifying and categorizing the diverse cell populations that comprise the brain, 2) understanding the input-output connectivities of these cell types, and 3) characterizing their physiological functions in circuit activity. Tools that allow for specific and systematic access to diverse human cell types are essential to these efforts.

In recent years, single-cell RNA sequencing (scRNA-Seq) studies have yielded transcriptomic cell type taxonomies of the rodent, non-human primate (NHP), and human brains[3–12]. In particular, human scRNA-seq data have demonstrated conserved as well as divergent features of cell type organization, brain areal specializations in cell composition[4,5], and evidence for genetic adaptations that may confer human-specific neural circuit architectures[3,7,9,13]. Importantly, these transcriptional data also serve as a catalog of genetic access points (i.e., "marker genes") that may enable the systematic targeting of human cell types for integrated functional studies. What has been lacking, however, are reliable, flexible and scalable tools

that leverage gene expression to provide experimental access to defined cell populations for human neuroscience studies[2,14].

Traditionally, experimental cell type access has relied on germline engineering approaches in model organisms (e.g., transgenic mouse driver lines)[15–18], which are inapplicable to human research[15–17]. More recently, enhancer-based viral vectors have been advanced as an alternative, cross-species approach to targeting neural cell types[19–22]. However, because enhancers work through DNA-protein interactions that are highly nuanced between target genes and cell types, they require large-scale efforts to identify and validate[21,23,24]. Furthermore, as enhancer tools are typically validated in mouse models, their generalizability and applicability to human cell types remain to be established. Adeno-associated viral capsid engineering is another potential strategy for cell type access[25], but capsid tropism at the resolution of specific cell types has yet to be demonstrated for neurons, particularly in human brain tissues[26–30].

Neurosurgical tissue specimens represent a promising experimental platform for tool development and human neuroscience research. Resected cortical tissues can be maintained *ex vivo* for weeks in organotypic culture preparations, which maintain local tissue cytoarchitecture, cell transcriptomic profiles, and neurophysiological activity[31,32]. *Ex vivo* human tissues have been used for a variety of live, semi-chronic research applications, such as the characterization of human disease pathogenesis[33], testing of emerging therapeutic approaches[34,35], and validation of novel experimental tools[21,22,36]. *Ex vivo* tissues have also been increasingly utilized for morphological and electrophysiological studies of human neurons[37–41] with, in some cases, subsequent analyses of cell transcriptomic profiles[6,42–45]. By enabling researchers to overlay cellular functional data onto human transcriptomic datasets, this set of approaches has enabled an initial multi-modal profiling of some human brain cell types. However, previous studies sampled human neural populations largely based on their soma shape and laminar position[6,46,47], or broad cell classes using broadly active enhancer viral vectors[19–21]. The lack of specific and effective methods for accessing molecularly defined cell types or subpopulations severely limits the basic and pre-clinical research potential of the human *ex vivo* tissue preparation.

We recently invented an orthogonal technology that uses a RNA and translation-based method to achieve cell type-specific targeting across diverse organisms[48]; two independent teams described essentially similar methods, and termed them RADARS[49] and RADAR[50]. CellREADR - Cell access through RNA sensing by Endogenous ADAR (adenosine deaminase acting on RNA) - is a programmable RNA sensor-effector technology that couples the detection of a cell-defining RNA to the translation of a user-selected effector protein; this coupling is achieved through an ADAR-mediated A-to-I editing mechanism ubiquitous to metazoan cells. In a prior study we demonstrated CellREADR-mediated monitoring and manipulation of neurons in behaving mice, characterized CellREADR sensor and effector properties in human cell lines, and provided a first proof-of-principle for CellREADR transduction in *ex vivo* human brain tissues[48]. Our initial findings highlighted CellREADR's unique programmability, flexibility and scalability as a tool for RNA-based cellular access. These features make CellREADR a

promising technological bridge for advancing from human cellular transcriptomic datasets towards functional investigations of human neural cell types.

In this study we demonstrate CellREADR's utility for accessing, monitoring, and manipulating marker-defined cell types in *ex vivo* human brain. We designed CellREADR constructs to provide experimental access to *CALB2* (calretinin) GABAergic interneurons and *FOXP2* (forkhead box protein P2) glutamatergic projection neurons in the temporal neocortex. Following histological, electrophysiological and transcriptomic characterizations of CellREADR-labeled neurons, we used PatchSeq techniques to cross-validate CellREADR targeting and perform molecular alignment of the experimentally accessed cells onto published transcriptomic reference atlases. We further performed optical stimulation and calcium imaging in *CALB2* and *FOXP2* populations to probe human cortical microcircuits. Together, these experiments define a novel and transformative approach for cell type-specific access, manipulation and functional monitoring in the human brain, *ex vivo*.

Results

Deploying CellREADR to target RNA-defined cell types in *ex vivo* human cortex

We used an organotypic slice preparation to study CellREADR applications in human cortical tissues (Figure 1A). Live tissue specimens were donated by epilepsy surgical patients and collected from non-diseased areas adjacent to known seizure foci (proximal, non-diseased tissues are minimally removed during surgery to access epileptogenic areas). Patient demographics and specimen details are presented in Table 1.

We designed both singular and binary CellREADR vectors for use in human tissues (Figure 1B). In the singular vector system, a human synapsin promoter (hSyn) drives expression of the sensor and effector RNAs; this vector directly couples RNA sensing to the translation of a chosen experimental effector (e.g., a fluorescent reporter). In the binary system, the sensor RNA first triggers the translation of a transcription activator tTA2 from the READR virus, which then activates the transcription of a TRE-driven effector gene by the Reporter virus. The binary system provides amplification of payload expression and also enables combinatorial pairing of READR and Reporter vectors to direct differential expression of effectors in different cell types.

We first produced CellREADR sensors for various interneuron and projection neuron marker genes (*VGAT*, *LAMP5*, *CALB2, SST*, *PVALB, UNC5B, CUX1, FOXP2*) and used them to express mNeonGreen (mNeon) in cells of the human cortex. Our initial screenings showed promising expression patterns across cell populations with characteristic morphological features (example images, Figure 1C). We elected to pursue more detailed investigations using the *FOXP2* and *CALB2* sensors, given data suggesting human brain specializations may be reflected in populations that express these genes.

FOXP2 is implicated in human language disorders[51,52], aberrant song learning in songbirds[53], and impairments in fine motor learning in mice[54]. In rodents, *FOXP2* expression is restricted to cortical excitatory neurons in deep layers[55], however, *FOXP2* is expressed more widely across

cortical lamina in humans[48,56]. Consistent with this, after applying a binary *FOXP2* CellREADR system to neocortical slices, we observed mNeon epifluorescence in pyramidal cells of both deep and superficial cortical layers (Figures 1C-E). To assess the specificity of *FOXP2* CellREADR transduction, we performed immunohistochemistry to quantify co-labeling of READR mNeon with cellular FOXP2 7 days after virus application (Figure 1F). Across tissues from 5 subjects, the mean specificity of the *FOXP2* READR labeling (percentage of mNeon+ cells co-labeled with FOXP2) was 75.4 ± 2.2% (Figure 1F-G).

In the human cortex, *CALB2* expression is largely restricted to supragranular GABAergic interneurons that originate from the caudal ganglionic eminence (CGE), primarily *VIP* subclass interneurons[57–59]. There is evidence for an increased abundance of CGE interneurons (versus medial ganglionic eminence interneurons) in humans and non-human primates, as compared to mice[3,7,9], with some studies suggesting a specific expansion of *CALB2* populations[57,60,61]. Using a binary *CALB2* READR system in human neocortical slices, we observed a pattern of mNeon labeling concordant with prior descriptions of *CALB2* expression. Compared to *FOXP2* READR labeling, *CALB2* READR expression was generally observed in outer cortical layers (Figures 1C-E). *CALB2* READR-labeled cells also exhibited morphologies distinct from *FOXP2* READR-labeled cells, with small somas and vertically oriented, bipolar or multipolar dendritic processes (Figure 1C). The specificity of *CALB2* READR transduction, as tested by immunohistochemistry in tissues from 7 subjects, was 72.5 ± 3.3% (Figures 1F-G).

To benchmark the binary *CALB2* CellREADR approach, we compared READR labeling to that achieved by an enhancer virus recently used for pan-interneuron targeting in human neocortex, DLX2.0[20] (Figure 1H). Of cells labeled by the DLX2.0-YFP virus, we found that 43.1 ± 6.0% co-expressed CALB2 (Figure 1J), consistent with prior evidence that DLX2.0 transduces broadly across GABAergic cell subclasses[42]. Likewise, as compared to *CALB2* CellREADR labeling, which was noted primarily in supragranular layers, DLX2.0 virus expression was more evenly distributed throughout cortical layers (Figure 1I). Although the binary *CALB2* CellREADR vector theoretically targeted a more restricted population of interneurons, it labeled greater numbers of cells than the DLX2.0 virus, suggesting its greater efficiency for transduction (Figure 1K; *CALB2*-READR, 34.5 ± 8.0 cells/mm^2, DLX2.0-YFP, 14.8 ± 2.8 cells/mm^2; Welch's t-test, $p = 0.0322$). Taken together, our findings with *FOXP2* and *CALB2* viruses indicated CellREADR's strong efficacy and specificity for targeting RNA-defined populations of human neurons.

PatchSeq validation of *CALB2* CellREADR targeting

To further validate CellREADR targeting and gain a multimodal characterization of some of the cells accessed by the *CALB2* READR, we performed PatchSeq on a limited number of labeled cells. Five to 11 days after the application of singular or binary *CALB2* READR vectors to slices of human temporal neocortex, we targeted mNeon+ cells for patch clamp electrophysiology, biocytin filling, and nuclear extraction. After performing RNA-seq on the nuclear aspirate, we applied an open sequencing analysis pipeline[62] to map queried cells onto a reference transcriptomics-based taxonomy of human middle temporal gyrus (MTG) interneurons[59] (Figure 2A).

As expected, our RNA-seq analysis detected *CALB2* transcripts in nearly all mNeon+ patch-targeted cells (18/19, 94.7%; Figure 2B). Notably, this exceeded the specificity of *CALB2* READR targeting measured by immunohistochemistry (Figure 1G), suggesting that incomplete sensitivity of CALB2 immunostaining may have underestimated the specificity of the *CALB2* READR. These RNA-seq results also indicate the CellREADR sense-edit mechanism did not grossly disrupt expression of the *CALB2* target gene. Based on existing transcriptomics data[59] (Figure 2A), which demonstrate that *CALB2* is expressed almost exclusively by *VIP* subclass interneurons, we hypothesized that *CALB2* READR-targeted cells would also express the interneuron class marker, *GAD1*, as well as *VIP*, but not markers of other cortical interneuron subclasses, such as *LAMP5*, *SST*, and *PVALB*. In accordance, transcripts of *GAD1* were detected in the majority of sampled cells (14/19, 73.7%), while *VIP* was detected in a somewhat smaller fraction (9/19; 47.4%); by contrast, transcripts of *LAMP5, SST, PVALB* were rarely observed in *CALB2* READR-targeted cells (Figure 2B). Looking beyond single gene expression, essentially all cells (18/19; 94.7%) mapped transcriptomically to types within the *VIP* subclass of MTG interneurons (Figures 2A and 2B). Of cells that mapped to the *VIP* subclass, one-third (6/18; 33.3%) were categorized as *PAX6 SYT6* type, while the remaining two-thirds (12/18; 66.7%) were mapped to other *VIP* types. In total, 10 of 21 previously annotated transcriptomic types of *VIP* interneurons[63] were represented amongst the 19 cells sampled by *CALB2* READR targeting. These results together indicate that CellREADR specifically targeted *CALB2* populations and, thereby, effectively accessed *VIP* interneurons.

Electrophysiology data from 17 of the 19 cells studied with RNAseq passed quality checks, and the morphologies of 7 cells were recovered for tracing. *CALB2* READR-targeted neurons largely showed a steep gain relationship between injected current and firing frequency, with many cells exhibiting firing frequencies exceeding 40Hz (Figure 2C). Qualitatively, cells that clustered within the same transcriptomic type nevertheless exhibited differences in their electrophysiological features. For example, within READR-targeted cells identified as *PAX6 SYT6* type, we observed two distinct patterns of input-output responses (Figure 2C), as well as similarly variable responses to hyperpolarization (Figure 2D). These basic phenotypic observations were consistent with recent human interneuron PatchSeq data[42], and generally align with prior observations that cell transcriptomic types do not necessarily express type-specific physiological features. As expected, however, we did observe some relationships between ion channel subunit expression and membrane physiology[37]. The expression of BK channel subunits, for example, correlated with both the depth of the fast afterhyperpolarization and the action potential duration, as would be expected given the function of this channel[64,65] (Supplemental Figure 1). Morphologically, reconstructed neurons were located in Layers 2-5, and they exhibited diverse dendritic and axonal distributions. Six of 7 cells projected dendrites vertically, while the other recovered cell's dendrites were oriented horizontally (Figure 2F). These morphologies are likewise generally consistent with *VIP* subclass morphologies[42].

CALB2- and *FOXP2-targeted* neurons exhibit distinct physiological profiles and spontaneous activities

After gaining evidence for CellREADR specificity through immunostaining and sequencing analyses, we proceeded to a more detailed physiological characterization of neurons targeted

by *CALB2* and *FOXP2* READRs. Applying a panel of electrophysiological readouts used to construct prior human cellular atlases[42,43,66], we recorded electrophysiological properties from 59 *CALB2* READR-targeted cells (n=8 subjects) and 46 *FOXP2*-targeted cells (n=7 subjects). We first measured intrinsic membrane properties and noted group differences in membrane capacitances (*CALB2*: 31.72 ± 3.35 pF; *FOXP2*: 88.46 ± 9.05 pF, Mann-Whitney p<0.0001) and input resistances (*CALB2*: 0.280 ± 0.041 MΩ; *FOXP2*: 0.082 ± 0.018 MΩ, Mann-Whitney p<0.0001) of cells labeled by *CALB2* and *FOXP2* READRs (Figure 3A). Hyperpolarizing sag ratios (*CALB2*: 0.18 ± 0.02; *FOXP2*: 0.15 ± 0.02) and resting membrane potentials (*CALB2*: -42.54 ± 1.41 mV; *FOXP2*: -45.71 ± 2.02 mV) did not differ between targeted cells (Figure 3A). We also characterized active membrane properties by quantifying cellular input-output responses; these measures included the rheobase, gain, and maximal firing frequency (Figure 3B). *CALB2*-targeted cells showed more variability in the shape of their input-output functions, with many neurons exhibiting low rheobase, high gain, and high maximal firing frequency (41/59 (65%) with maximum firing frequency >40Hz), and a smaller subset of neurons demonstrating high rheobase, low gain, and low maximal firing frequency. *FOXP2*-targeted cells were of more uniform firing behaviors, with relatively shallow gain slopes and maximal firing frequencies typically under 40Hz (11/46 (24%) with maximum firing frequency >40Hz). Statistically, rheobases (*CALB2*: 37.9 ± 5.9 pA; *FOXP2*: 110.8 ± 14.0 pA, paired Mann-Whitney p<0.0001), gains (*CALB2*: 0.55 ± 0.04 Hz/pA; *FOXP2*: 0.18 ± 0.03 Hz/pA, paired t-test, p<0.0001), and maximal firing frequencies (*CALB2*: 53.94 ± 2.57Hz, *FOXP2*: 36.15 ± 4.03Hz, Welch's t-test p=0.001) differed between *CALB2*- and *FOXP2*-targeted cells.

We also measured single action potential parameters, including threshold, peak, half-width, and fast afterhyperpolarization from targeted cells (Figure 3C). All single APs from the *CALB2* and *FOXP2* cells were aligned on the rising slope and averaged. *CALB2*-targeted cells had narrower action potentials with both shorter half-widths (*CALB2*: 1.14 ± 0.05 ms; *FOXP2*: 1.49 ± 0.01 ms, Welch's t-test p=0.006) and durations (not shown; *CALB2*: 2.35 ± 0.01 ms; *FOXP2*: 2.99 ± 0.17 ms, Mann-Whitney p=0.003). The *CALB2* population had a larger fast afterhyperpolarization (fAHP; *CALB2*: -23.75 ± 1.08 mV; *FOXP2*: -20.45 ± 0.91 mV, Welch's t-test p=0.009); a subset of the *FOXP2*-targeted neurons were notable for their pronounced afterdepolarizations. Neither the action potential thresholds (*CALB2*: -32.66 ± 1.03 mV; *FOXP2*: -32.81 ± 1.40 mV) nor the action potential heights (*CALB2*: 34.67 ± 1.40 mV; *FOXP2*: 33.80 ± 1.70 mV) statistically differed between the targeted populations. In sum, the differences in the intrinsic properties, firing phenotypes, and action potential dynamics between the *CALB2*- and *FOXP2*-targeted cells are consistent with the specific targeting of interneurons and projection neurons, respectively[67,68].

We also used patch clamp to measure activity from *CALB2*- and *FOXP2*-targeted cells at rest, in order to assess synaptic inputs and cellular activity in the slice network. In cells of both target populations, we observed excitatory and inhibitory postsynaptic potentials (EPSPs and IPSPs; Figure 3D), as well as action potential firing (Figure 3E). *CALB2*-targeted neurons were often found to fire from resting membrane potential, whereas a smaller fraction of *FOXP2*-targeted cells exhibited this behavior (*CALB2*: 40/59 cells (67.8%), *FOXP2*: 12/43 cells (27.9%); Fisher's exact test p<0.001; Figure 3F). Spontaneous activity, measured as the

frequency of spontaneous action potential firing, differed between *CALB2- and FOXP2*-targeted populations (*CALB2*: 1.73 ± 0.40 Hz; *FOXP2*: 0.42 ± 0.21 Hz, Mann-Whitney p<0.0001, Figure 3G). While EPSPs were often observed in recorded cells, it was not clear whether action potentials were driven by synaptic inputs, intrinsic membrane depolarization past threshold, or a combination of both. As *CALB2*-targeted cells exhibited lower rheobases and higher input resistances than *FOXP2*-targeted cells (Figures 3A-B), they are expected to respond more readily to synaptic inputs, which could explain the higher firing observed in this set of cells, as compared to the *FOXP2*-targeted neurons.

Cell type-specific optical manipulation of human neurons with CellREADR

We next explored CellREADR functionality for cellular manipulation and interrogation of human microcircuits. We designed a binary vector system consisting of either *CALB2*-tTA2 or *FOXP2*-tTA2 paired with a TRE-driven channelrhodopsin variant, ChIEF[69], and then delivered viruses to neocortical slices. We first used patch clamp to assess optically evoked action potential firing in *CALB2*-ChIEF and *FOXP2*-ChIEF cells. In all *CALB2*-targeted cells (n=6), we observed reliable, light-entrained action potentials (Figure 4A); each of these cells was able to follow light pulses with action potentials at frequencies >25Hz (data not shown). By contrast, optical stimulation of *FOXP2*-ChIEF cells evoked membrane depolarizations of 2-9mV, but it did not elicit action potentials (n=10 cells; Figure 4A). These differences in light responsiveness were somewhat expected based on our intrinsic physiological characterizations of these populations (Figure 3), which indicated that *FOXP2*-targeted cells are less excitable than *CALB2*-targeted cells. We next focused on additional optogenetic experiments with *CALB2* READRs.

It has been reported that calretinin interneurons project onto local inhibitory and excitatory populations in rodent cortex[70] and hippocampus[71]; in non-human primate visual cortex CALB2+ cells have been found to target glutamatergic neurons in deeper layers[72]. To functionally interrogate the synaptic targets of *CALB2* neurons in human neocortex, we recorded from pyramidal neurons and interneurons to measure optically-evoked postsynaptic currents (PSCs) from *CALB2*-ChIEF cells. Putative postsynaptic cells were labeled with complementary DLX2.0-YFP or hSyn-mCherry AAV vectors to label YFP+ interneurons and mCherry+ pyramidal neurons, respectively, for patch clamp recordings (Figure 4B). Representative optical inhibitory PSCs (oIPSCs) in slice interneurons and pyramidal neurons are depicted in Figure 4C. The latency, rise time, and duration of oIPSCs indicated that light stimulation produced monosynaptic GABA release onto the patched cells (Figure 4D).

We observed optical PSCs in both YFP+ interneurons and mCherry+ pyramidal neurons (4/12 DLX2.0-YFP+ cells (33.3%) and 4/12 hSyn-mCherry+ cells (33.3%)). When performing voltage clamp measures, we found that *CALB2*-ChIEF activation evoked inhibitory, but not excitatory, responses in interneurons (4/12 DLX2.0-YFP+ cells (33.3%) exhibited inhibitory responses and 0/12 cells exhibited excitatory responses upon *CALB2*-ChIEF activation; Figure 4E). By contrast, *CALB2*-ChIEF activation evoked inhibitory responses in some pyramidal neurons, and excitatory responses in others (2/12 hSyn-mCherry+ pyramidal cells (16.7%) exhibited inhibitory responses and 2/12 cells (16.7%) exhibited excitatory responses *CALB2*-ChIEF activation; Figure 4E). It is unclear whether this observation of excitatory responses in

pyramidal neurons reflected glutamate release from a subset of *CALB*+ cells or off-target expression of the CellREADR ChIEF. Notably, our PatchSeq experiments indicated that at least a subset of *CALB2*-targeted cells, particularly those that align with the PAX6 SYT6 transcriptomic subtype, appear to express both vesicular glutamate transporter (*SLC17A7*) and glutamate decarboxylase transcripts (*GAD1* and *GAD2*); Figure 2B)); additionally, a small subset of human MTG excitatory neurons express low levels of *CALB2* (Supplemental Figure 2)[59]. These results thus may reflect primate or human specific features of *CalB2* neurons distinct from those of rodents. We did not observe both excitatory and inhibitory responses to *CALB2*-ChIEF activation in the same pyramidal cell.

Cell type-specific monitoring of population activity with CellREADR

We also investigated CellREADR functionality for imaging neuronal population activity in *ex vivo* human cortex. We used the binary CellREADR system to express the genetically encoded calcium indicator, GCamp7f, in *CALB2* and *FOXP2* target populations. To establish how calcium signals reported membrane depolarizations and action potentials in this system, we first measured fluorescence signals at individual GCaMP7f+ cells under concurrent patch clamp (Figure 5A). In both target populations we observed a linear relationship (R^2 of the linear fit *CALB2*: 0.84; *FOXP2*: 0.93) between the GCaMP ΔF/F measure and the frequency of action potentials evoked by current injection. This response curve theoretically enables the quantitative calcium imaging of action potential firing. During current clamp recordings, we also observed both prolonged spontaneous subthreshold membrane depolarizations and action potentials in the same cell; these electrophysiological events were reflected by distinct GCaMP signals with different rise times (Tau_{3AP} = 390 ms, $Tau_{Depolarization}$ = 1760 ms, Tau_{1AP} = 202 ms, Figure 5B).

As we had observed frequent spontaneous action potential firing in *CALB2*- and *FOXP2*-targeted neurons under patch clamp (Figure 3E-G), we expected GCaMP imaging would detect population activity in the slice preparation. Indeed, when performing wide field imaging of neocortical slices without stimulating agents, we observed baseline spontaneous activity in both populations (representative images of GCaMP labeling, Figures 5C). Representative time series of ΔF/F signals for *CALB2*- and *FOXP2*-targeted populations are shown in Figure 5D. Qualitatively, spontaneous population activity patterns varied between slices, even across slices that were prepared from the same subject's tissue. Action potentials (reflected by fast-rising calcium transients of varying amplitudes (as in Figures 5A-B)) were observed in multiple cells from the READR-targeted populations (Figure 5D). We also observed prolonged calcium signals (as in Figure 5B) that occurred simultaneously in many cells (Figure 5D). These latter events may reflect local neuromodulatory signals or enhanced within-population connectivity that act across the recorded population. Coordinated activity was more prominent in *FOXP2*-targeted populations than in *CALB2*-targeted populations, as reflected by a cross-wise correlation analysis of calcium signal patterns (Pearson's rho value for population correlation, 0.639 for the *FOXP2-targeted* cells, 0.402 for the *CALB*-targeted cells; translated into Fisher's Z values for statistical comparison, p=0.03; Figure 5E).

Differential gene expression analyses of an existing RNAseq database[59] indicate the expression of nicotinic acetylcholine receptor subunits differs significantly between *CALB2*+ and *FOXP2*+ neurons. In particular, cholinergic receptor nicotinic alpha 2 subunit (*CHRNA2)* is expressed in a higher percentage of *CALB2*+ neurons (52.5%) than *FOXP2*+ neurons (1.1%), and at an approximately 1000-fold higher expression level (p-adj = 0), though *CHRNA4*, *CHRNA6*, and *CHRNA7* also showed enrichment in *CALB2*+ over *FOXP2*+ neurons (p-adj = $8.75x10^{-7}$, $3.22x10^{-94}$, $1.27x10^{-191}$, respectively). Of nicotinic acetylcholine receptor subunits, only *CHRNA1* showed enrichment in *FOXP2*+ neurons (2.8% of FOXP2+ neurons, with approximately 100-fold enrichment over *CALB2*+ neurons, p-adj = $6x10^{-3}$). We thus hypothesized we might observe differential calcium signal responses to nicotinic acetylcholine receptor signaling between these populations in the slice model. We compared transients from cells in the absence and presence of bath nicotine in 3 slices from each condition, and observed a trend towards increased engagement of *CALB2*-targeted cells in population activity (calcium signaling events were detected in 19/100 *CALB2*-targeted cells (19%) under baseline conditions, and in 30/100 cells (30%) following nicotine application; calcium signals were detected in 32/64 *FOXP2*-targeted cells at baseline (50%) and in 33/64 cells (51.6%) following nicotine application; *CALB2,* p=0.09 and *FOXP2,* p=0.999 by Fisher exact test, Figure 5F). In active cells, we also observed a trend towards larger calcium transients following nicotine application in *CALB2*-targeted cells (*CALB2*-targeted cells: 2.4 ± 1.1 ΔF/F under baseline conditions, 6.0 ± 2.6 ΔF/F following nicotine application; *FOXP*2-targeted cells: 1.6 ± 0.4 ΔF/F under baseline conditions, 1.0 ± 0.4 ΔF/F following nicotine application; 2-way ANOVA interaction, p=0.08; not shown).

Discussion

To advance our understanding of the brain and devise targeted human neurotherapies, it will be essential to investigate the design and function of human neural circuits at cell type-resolution. *Ex vivo* human tissues hold significant potential as a platform for studying human neural circuits, but the lack of facile and scalable tools for targeting human cell types has thus far limited the discovery and translational impacts of this model system. Here we demonstrate that the CellREADR RNA sensor-effector technology enables specific, effective, and programmable recording and manipulation of marker-defined neuronal types in *ex vivo* human brain tissue. Our initial findings highlight CellREADR's promise as a genetic tool for human neuroscience and therapeutic applications.

Specificity is of foremost importance for cell type-targeting technologies. We found that the specificity of our *CALB2* and *FOXP2* sensors exceeded 75% specificity, based on immunohistochemical validations (Figure 1). This may have underestimated true specificity of the sensors, as immunohistochemistry is technically challenging in human slice cultures due to factors such as lipofuscin autofluorescence and reagent availability (e.g., many commercial antibodies are not necessarily raised against human antigens). Indeed, our single-cell PatchSeq, which assessed comprehensive transcriptional profiles of READR-labeled cells, demonstrated 95% specificity (18/19 cells tested) for the *CALB2* sensor (Figure 2). Of note, for a given marker gene transcript, READR specificity can theoretically be increased by using

multiple sensor sequences in the same construct, each with editable STOP codons[48]. In the current study, our *CALB2* and *FOXP2* READRs each contained just a single sensor/STOP codon, yet both achieved impressive specificity. These results demonstrate the robustness of CellREADR design for targeting human brain cell types. Our ongoing testing of multiple sensors for *PVALB*, *SST*, and *UNC5B* has yielded promising READRs for other cell types (Figure 1C), but quantitative validation awaits further testing through RNA *in situ* hybridization, antibody staining, or RNA-seq analysis. Looking ahead, our major long-term goal is to implement large-scale screens of sensor libraries, then to systematically test a number of promising sensors for each target RNA in human cell culture systems and *ex vivo* tissues. Such studies will provide feedback for the optimization of a sensor design algorithm, and ultimately generate a comprehensive set of human CellREADRs.

Payload expression is also critical to the functionality of a cell-targeting tool. While CellREADR can be delivered using lipid nanoparticles for *in vitro* transcription[73,74], here we focused on DNA and AAV-based delivery, which may be better-suited for long-term payload expression in brain cells. In our singular vector design, direct coupling of payload translation to the sensor yielded mNeonGreen fluorescence in live tissues 6-9 days after virus application. The binary vector design substantially enhanced payload expression through tTA-TRE transcriptional amplification, achieving live mNeonGreen labeling within 3 days of virus application. Indeed, the binary vector system expressed fluorescent proteins, calcium indicators and opsins at levels that enabled targeted patch clamp (Figures 2 and 3), optogenetic manipulation (Figure 4), and calcium imaging (Figure 5) of human cell types. As CellREADR is orthogonal to and complementary with transcriptional enhancer-based tools, we were able to use it together with an interneuron class-specific enhancer, DLX-2.0, to investigate human interneuron synaptic connectivity (Figure 4). Our optogenetic data extend from previous studies[19,36,38] to provide the first proof-of-principle for cell type-specific optical interrogation of synaptic connectivity in human tissues. Likewise, our CellREADR calcium imaging experiments (Figure 5) also stand as the first demonstration of cell type-specific calcium imaging in human microcircuits[38].

Vector selection likewise influences delivery and expression of the genetic payload. Virus serotype must confer tropism to the target population of interest, and should be validated from the outset[25]. The AAV-PHP.eB (as in Lee et al.[42]) and rAAV2-retro (here) appear to have broad tropism for human neuron classes, and thus may be paired with CellREADR for targeting neuronal types. Similarly, the promoter used to drive READR expression must be active in the targeted cells. Here we used a human synapsin promoter[75], which appears to be broadly active in mammalian neurons. Prior to pairing with CellREADR, candidate promoters should likewise be validated in populations that include the target cell type.

To date, transcriptional enhancer-based methods are the best-described strategy for targeting NHP and human brain cell populations. For example, the DLX2.0 enhancer[21] provides cross-species (mouse, NHP, human) access to the cortical GABAergic interneuron class[42], and the mouse *Scn1a* enhancer targets the parvalbumin+ subclass in several mammalian species, including humans[19]. Additional interneuron subclass-specific enhancers have recently been identified through screening and validation in mice, and some of these may be of utility for

targeting human interneurons[76]. With advances in single cell epigenome analysis and large-scale enhancer discovery, this approach will continue to yield useful cell type-specific tools, which could also be combined with CellREADR sensors in the same vector for increased targeting specificity. On the other hand, as enhancer screening and validation are typically carried out in rodents, the degree to which enhancers are conserved and thus effective in human cellular "homologs" remains to be established, despite some encouraging cases of conserved activity[19,21,22,76]. Also, recent findings indicate the human brain contains cell transcriptional types that are unique from those in other mammals[9,46,47]. Thus, studying these unique cell types and their related circuits may require dedicated tools; in this context, CellREADR RNA sensors can be scalably designed to directly target these cells' specific RNA markers.

In summary, our results demonstrate that the CellREADR RNA sensor-effector technology can achieve specific, effective, and versatile monitoring and manipulation of human neuron types in *ex vivo* brain tissues. Significant efforts, including large-scale sensor screens in cell cultures and organotypic brain preparations, will be necessary to establish comprehensive sensor tools for human brain cell types. This is required to leverage the inherent programmability of CellREADR, which theoretically enables highly refined access through the intersectional targeting of multiple markers, as well as the differential delivery of effectors to multiple distinct cell types in the same tissue preparation. Synergistic with and complementary to capsid engineering and enhancer-based approaches, CellREADR is poised to substantially accelerate cell-type-specific access for the *ex vivo* study of human neural circuits in health and pathological states. Together, these technologies will elevate the human *ex vivo* tissue system as a foundational basic research platform and a translational bridge towards cell-type and circuit specific therapeutics in the human brain.

Methods

Plasmids

All the CellREADR sesRNAs were generated using gBlock synthesis (Integrated DNA Technologies). Vector backbones were linearized using restriction digestion, and DNA fragment inserts were generated using PCR or gBlock synthesis (Integrated DNA Technologies).

sesRNA design

The sensor RNAs (sesRNAs) used in this study were designed as previously described[48]. In brief, we designed 2-6 sesRNAs for both coding sequence and 5'UTR region of each target gene, depending on the gene length, and cloned the synthesized sesRNA into CAG-BFP-sesRNA-GFP construct. We also synthesized the target gene (coding sequence and 5'UTR) using gBlock and cloned to expression plasmid with CAG promoter. We tested the efficiency and specificity of each sesRNA in HEK cells using methods we have previously described[48], and used the sesRNA with highest specificity for further study.

Viruses

CellREADR viruses were designed and prepared using methods we have previously described[48]. In brief, for production of READR and reporter viruses, HEK293T cells were transfected with READR or Reporter plasmids, AAV serotype plasmids, and pHelper using PEI MAX (Polysciences, 24765). Seventy-two hours after transfection, the cells were collected in cell culture medium, and centrifuged at 4,000 rpm for 15 min. The supernatant was discarded, the pellet was resuspended in cell lysis buffer, frozen, and thawed three times using a dry ice/ethanol bath. Cell lysate was centrifuged at 4,000 rpm for 20 min. Contaminating DNA in the supernatant was removed by benzonase treatment. The crude viral preparation was loaded onto an iodixanol density gradient and spun at 60,000 rpm for 90 min using a Beckman Ti70 rotor. After the centrifugation, 3–4 ml of crude viral preparation was collected from the 40–60% layer with an 18-gauge needle attached to a 10-ml syringe. The viral crude solution was concentrated to 200–250 µl using the Amicon Ultra-15 centrifugal filter (100 kDa), washed with 8 ml PBS once, and concentrated to an appropriate volume. AAVrg-hSyn-mCherry (Addgene #50459) and AAVrg-DLX2.0-YFP (Addgene #163505) were used to target either pyramidal neurons or interneurons, respectively.

Human organotypic sample preparation and culture

Human cortical tissue was obtained from neurosurgical treatments for epilepsy. Non-diseased tissue, which was surgically removed to access areas of disease pathology, was used for this study. All subjects provided informed consent and donated tissue under an IRB Protocol (00103019) at Duke University. Biological sex was recorded, but gender identity was not collected. Patient demographics are listed in Table 1.

Organotypic slices were prepared according to published methods[31,32]. Dissection solution contained (in mM): 75 sucrose, 87 NaCl, 25 glucose, 26 $NaHCO_3$, 2.5 KCl, 1.2 NaH_2PO_4, 10 $MgCl_2$, 0.5 $CaCl_2$, bubbled with 95/5% O_2/CO_2 (pH 7.4). Cortex was carefully dissected under ice cold (~4C) oxygenated dissection solution to remove the pia. Single gyri were blocked for slicing and cut at 350µm thickness on a vibratome. Slices were rinsed in Hank's Buffered Saline and plated on PTFE membranes (Millipore, cat. # PICMORG50) in 6 well plates. Tissue was cultured in a conditioned media[31]. Conditioned media also contained antibiotic/antimycotic (1X, Gibco by ThermoFisher) for the first 7 days *in vitro*, and cyclosporine (5µg/mL) for the entire culture period. HEPES (20mM) was added to the media for the first hour after slice preparation. Slices were cultured in an incubator at 35C with 5% CO_2 and 5% humidity. Virus-mediated expression of fluorescent reporters was monitored from DIV 3 onward; slices were used for immunohistochemistry, patch clamp, and calcium imaging experiments between DIV 4 and DIV 16.

Virus application

On the day of tissue donation, after slicing and plating the tissue on semi-permeable membranes and after the 1 hour incubation in HEPES containing media, viruses were directly applied to the surface of the slice. Viruses were diluted in media (CellREADRs, 1:8 dilution; reporters, 1:6 dilution; commercially available viruses, 1:10 dilution), and 7µL of the virus solution was applied to slice grey matter. Plates were carefully returned to the incubator and left undisturbed overnight.

Immunohistochemistry

After 7 or 10 days of incubation, or following patch clamp recording, cortical slices were fixed overnight in 4% PFA, then rinsed in PBS and stored from 1-7 days in PBS with azide. For biocytin recovery or colocalization IHC, tissue was permeabilized in PBS with 10% TritonX100, 5% NGS, and 100uM glycine 2 hours at room temperature on a shaker plate.

Primary antibodies were incubated 48 hours at 4C; secondary antibodies were incubated for 24 hours at 4C. Biocytin was developed with either Alexa647 conjugated streptavidin, or with a silver stain. Large overview images of native mNeon fluorescence were made on a Leica SP8 upright confocal microscope, or a Keyence BZ-X800 with a 10X or 20X objective.

The following antibodies were used for immunohistochemical labeling of mNeon, mCherry, FoxP2, Calretinin and NeuN: mouse anti-mNeon Ab 1:500, Proteintech 32f6; chicken anti-mCherry Ab 1:500, Origene TA150127; rabbit anti-FoxP2 Ab 1:500, Abcam ab16046; rabbit anti-Calretinin Ab 1:500, Swant CR7697; mouse anti-NeuN Ab 1:500, Cell Signaling #94403S. Secondary antibodies were Alexa488, Alexa594, or Alexa647 against the appropriate species (Invitrogen). Slices were mounted using a medium containing DAPI.

Some slices were selected for chemical clearing to enhance imaging deeper into the slice and reduce lipofuscin autofluorescence. These slices were incubated in thiodiethanol (TDE) solution of 30% for 35 minutes, 60% for 35 minutes, then 75% for 10 minutes. Slices were mounted in a 300µm thick spacer ring (SunJin Labs, iSpacer, IS307), then the remaining volume was filled with 75% TDE before coverslip placement.

Image analysis for colocalization & cell location

Immunohistochemistry measurements of CellREADR specificity were performed by immunostaining against either CALB2 or FOXP2 protein and CellREADR mNeonGFP. Maximum projection images of small z-stacks (40-60µm total depth) were used for manual counts of mNeon-labeled cells and CALB2 or FOXP2 using the CellCounter Plugin in FIJI. Colocalization was expressed as the percentage of mNeon+ cells that also expressed the marker protein of interest (CALB2 or FOXP2).

Electrophysiology

Slices were transferred to a heated recording bath (32-34C) on an Olympus BX-50 upright microscope. Recording solution contained (in mM): 118 NaCl, 3 KCl, 25 $NaHCO_3$, 1 NaH_2PO_4, 1 $MgCl_2$, 1.5 $CaCl_2$, 30 glucose fully saturated with 95/5% O_2/CO_2. Borosilicate patch pipettes were pulled with a resistance of 3.5-5.5 MΩ, and filled with an internal solution containing (in mM): 134 K-gluconate, 10 HEPES, 4 ATP-triphosphate Mg salt, 3 GTP-triphosphate Na salt, 14 Phosphocreatine, 6 KCl, 4 NaCl, pH adjusted to 7.4 with KOH for current clamp recordings For voltage clamp recordings (optogenetic stimulation of PSCs), the internal solution continued (in mM): 100 Cs-MeSO3, 40 CsCl, 4 MgCl2, 0.1 Na3-GTP, 4 Na-ATP, 10 Tris-Phosphocreatine, 10 HEPES, and 4 QX-314. Biocytin (0.5%) was added to the internal solution to allow for morphological identification after recording. Patched cells were held in whole-cell mode for a minimum of 10 minutes to ensure complete filling with biocytin.

Labeled cells were targeted for patch clamp under a 60X objective. Recordings were performed using an Axopatch 700B amplifier (Molecular Devices), and data were digitized (Digidata 1550B) and captured with pClamp 10 (Molecular Devices). Membrane voltage was recorded at 100k Hz and low-pass filtered at 10k Hz. Liquid junction potential was not corrected. Pipette capacitance and series resistance were compensated at the start of each recording and checked periodically for stability of the recording configuration. Intrinsic membrane properties (input resistance, capacitance) were measured with a -10pA current step. Rheobase was measured with a ramp current of 1s duration and 100-300pA final amplitude. Input-output curves were generated from a series of current steps starting at -100pA and increasing in 10pA increments until a maximum firing rate was elicited. Sag ratio was calculated from the -100pA step, and was the difference between the negative peak deflection from baseline and the steady-state voltage normalized to the peak deflection[63]. Data were analyzed using NeuroMatic and custom scripts in Igor Pro (Wavemetrics).

Optical stimulation experiments were performed by expressing either AAVrg-DLX2.0-YFP, AAV9-hSyn-GFP or AAV9-hSyn-mCherry in putative postsynaptic cells, and CALB2-ses1-tTA and TRE-ChIEF-YFP or TRE-ChIEF-tdTom CellREADR constructs in putative pre-synaptic populations. Cells that 1) expressed only the DLX2.0-YFP or hSyn-mCherry, and 2) were situated in areas of CellREADR labeling, were targeted for voltage clamp recordings. Blue light pulses (625 nm, 5 2ms-long pulses at either 10Hz or 50Hz) were triggered for 10 sweeps while recording membrane currents at -30mV (V_{rev} GABA) and at 0mV (V_{rev} Glu). If an optical response was detected in the average of the 10 sweeps, then glutamatergic blockers (20uM CNQX + 50uM AP-5) were bath applied to the slice and the optical stimulation was repeated to verify the neurotransmitter that was the source of the optical PSC.

Calcium Imaging

Four to 6 days after virus application, slices with robust GCaMP7f fluorescence were selected for experiments. Slices were placed in a bath chamber at 32C under a 10x objective and a high-power LED (Thor Labs) at 488nm. Videos of 60-90s duration were captured at a frame rate of 100ms with a Retiga Electro 1.4M pixel CCD camera (Teledyne Photometrics). FIJI was used to check the standard deviation projection of the video for spontaneous activity. If activity was detected, several videos were then captured in the same region, then a different area of the slice was imaged. Between 4 and 10 videos were captured from each field of view over the course of 10-15 minutes. Nicotine (300uM) was bath-applied to a subset of slices, then videos were recaptured 5 minutes later from the same field of view. After allowing nicotine to wash out for 15 minutes, baseline imaging was then performed at a new location.

One representative video of each field of view was selected if it 1) contained a relatively high density of labeled cells, 2) exhibited minimal motion artifacts, and 3) did not include the most active or least active period of activity that was measured. Data were analyzed with ImageJ (FIJI) and custom scripts in Igor Pro. If necessary, motion artifact was corrected with the Image Stabilizer plugin. Maximum projection images were used to select all neurons in the field of view for analysis (even non-active cells were analyzed). ROIs were assigned to each neuron, and intensity values over time were extracted for each ROI. Calcium signals were background subtracted and normalized to a baseline period that exhibited no activity. Co-activation was

calculated by a pairwise cross-correlation (Pearson's) of all the ROIs in the field of view. Pearson's correlation coefficients were converted to Fisher's z-values for comparison across slices and between groups.

Processing of cellular nuclei for PatchSeq

PatchSeq electrophysiology was performed using an internal solution that included (in mM): 110 K-gluconate, 4 KCl, 10 HEPES, 1 ATP-Mg, 0.3 GTP-Na,10 Na-phosphocreatine, 0.2 EGTA, 20µg/mL glycogen, 0.5% biocytin, and 0.5U/µL RNase inhibitor (Takara). The internal solution was prepared with RNase-free water, and stored in daily aliquots at -80C until use. Equipment and materials preparation and nuclei extraction followed previously published protocols[77]. Clean nucleus extraction was confirmed visually with both DIC and fluorescent images. Nuclei were stored at -80C in 10µL of lysis buffer with RNase inhibitor (40U/µL), and then processed for sequencing in batches (5-12 nuclei/batch). Nuclear RNA was processed into cDNA libraries using the SMART-Seq v4 Ultra Low Input kit (Takara) using 19 PCR cycles. Quality checks of the resulting cDNA were made on a Bioanalyzer (Agilent, High Sensitivity DNA kit). Nuclei that yielded >200pg/µL cDNA were sequenced. Borderline cDNA (concentrations just below 200pg/µL, and fragment sizes >500bp) were re-amplified with 3 rounds of PCR, rechecked for cDNA quality, and included in the sequencing set if the reamplification increased cDNA concentration above threshold.

RNA sequencing and transcriptomic analysis

cDNA sequencing was performed at the Duke Sequencing and Genomics Technologies core facility on an Illumina NovaSeq 6000 flow cell with a targeted sequencing depth of approximately 50 million reads per sample. Data were aligned to the human genome (GRCh38, annotations from ENSEMBL v106). Raw count matrices from aligned data were analyzed using the Allen Institute scrattch.hicat (version 1.0.0) package (https://github.com/AllenInstitute/scrattch.hicat) in R (2022.07.1 Build 554). Normalized counts were calculated as log2(counts-per-million reads per cell) for downstream analysis. Heatmaps for select genes were generated using the gplots package (version 3.1.3) in R.

Predicted transcriptomic cell type annotations were derived from a reference dataset of 15,928 nuclei from the human middle temporal gyrus (MTG) that underwent SMART-seq single nucleus RNA sequencing[59]. Annotation predictions were generated using scrattch.hicat (version 1.0.0) according to a standard data analysis pipeline (https://taxonomy.shinyapps.io/scrattch_tutorial/#section-overview). The reference MTG dataset was limited to interneuron clusters (class = GABAergic); cell class and cluster (i.e. Inh L1-3 PAX6 SYT6) were used to generate reference cluster names. The reference count matrix and the PatchSeq test count matrix were both normalized (log2(counts-per-million(raw matrix) +1)) and key cluster specific genes were selected using the "select_markers" function in scrattch.hicat. Cluster predictions for PatchSeq cells were then generated using the "map_sampling" function in scrattch.hicat (markers.perc=0.8, iter=100).

To investigate differential gene expression between *CALB2*+ and *FOXP2*+ neurons we utilized an existing single-nucleus RNA sequencing atlas from human MTG [ref55]. The atlas dataset

was reconstituted in Seurat via CreateSeuratObject, and then the raw count matrix was normalized and scaled via SCTransform with default parameters. The human MTG Seurat object was further subsetted for cells with non-zero expression of *CALB2* or *FOXP2*, yielding *CALB2*+ GABAergic neurons and *FOXP2*+ Glutamatergic neurons. Differential gene expression was then analyzed between these two populations via FindMarkers(object, ident.1 = "GABAergic, ident.2 = "Glutamatergic", only.pos = FALSE), yielding log2-fold changes in expression, percent gene expression in ident.1 and ident.2, and a p-value adjusted for multiple comparisons where p-adj <0.05 was considered significant differential expression. The list of differentially expressed genes was then manually investigated for significantly differentially expressed genes of interest related to neuromodulation (i.e. nicotinic acetylcholine receptor subunits).

PatchSeq morphological studies

For cortical layer identification, 4 sections from 4 subjects were labeled with DAPI and imaged from the pia to the white matter border. The density of nuclei delineated layer boundaries; the distances between each layer were calculated for the 4 samples and averaged to create a "typical" cortical layer map. Our cortical layer distances were as follows: L1-L2 boundary, 221.8µm, L2-L3 boundary, 383.9µm, L3-L4 boundary, 812.2µm, L4-L5 boundary, 1677.6µm, L5-L6 boundary, 2206.9µm, L6-WM boundary, 3549.5µm. This is a slightly deeper cortical average than reported elsewhere (2963µm)[37]. When a biocytin-filled cell was identified, the distance from the pia to the cell soma was measured, as was the underlying Layer 6-white matter boundary (these were measured along a line perpendicular to the overlying pia). Soma position was then calculated as a percent depth (0% is located at the pial surface and 100% is located at the Layer 6-white matter boundary. This normalized the depth position of the soma across slices. DAPI labeling was used as a secondary criterion to ascertain the soma laminar position.

For morphological tracings, biocytin-filled neurons were imaged using a 40x objective on a Leica SP8 upright confocal microscope (oil immersion, NA = 1.3). Tiled z-stacks containing cell dendrites and axons were captured at 1024x1024 resolution, with a z-step size of 1.0-1.2µm. Overview images were captured using a 10x objective to provide a reference for cell orientation relative to the pial surface. Images were traced using the automatic tracing plugin in Vaa3D[78] and converted to .SWC format. The automatic tracing function sometimes produced erroneous branching points, and so all traces were inspected and manually corrected using either the SNT plugin in FIJI, or neuTube, a plugin for Vaa3D. To orient the traces relative to the pial surface, corrected .SWC files were aligned in the SNT Viewer using the 10X overview images to position all cells vertically in the cortical column.

Statistical Analyses

All data values in the text are the mean +/- SEM; error bars in the figures indicated the SEM. Statistical tests were performed in GraphPad Prism. Data were checked for normality; normally distributed data were compared with t-test or ANOVA. Non-normal data distributions were compared with the Mann-Whitney U-test.

Figure Legends

Figure 1: Deploying CellREADR to target RNA-defined cell types in *ex vivo* human cortex

A) Human organotypic slice model. Human neocortical tissue specimens (here, middle and inferior temporal gyri; left) were sectioned into 350µm slices and cultured on semi-permeable membranes for up to 16 days in vitro (DIV; right). CellREADR AAV vectors were directly applied to slices on DIV 0.

B) Schematic of CellREADR design. In the single virus design (left), binding of the sensor RNA sequence to the target leads to ADAR-mediated editing of a stop codon positioned between the sensor and the effector, leading to expression of the downstream effector (here, mNeon). The binary system (right) uses a CellREADR virus (top right) to drive expression of tTA2 (Tet-Advanced transactivator) in the target cell. A reporter virus, designed to conditionally express a selected effector molecule (e.g. mNeon, ChIEF, GCamp7f, depending on experiment) under control of the Tet-Responsive Element (TRE), is also applied.

C) CellREADR targeting of diverse neuronal populations. Binary CellREADRs (mNeonGFP reporter) designed against Somatostatin (*SST*), Unc-5 netrin receptor B (*UNC5B),* Parvalbumin (*PVALB*), Forkhead box protein P2 (*FOXP2)*, and Calretinin (*CALB2*) were applied to slices of human neocortex. Slices were immunostained for mNeon 7 days after virus application. The CellREADR binary system led to robust expression of mNeon in differing laminar distributions and in cells of various morphologies. Dashed red boxes highlight the area depicted in the accompanying magnified image; pia and white matter (WM) are illustrated with dotted lines.

D) Histological analysis of *FOXP2* and *CALB2* CellREADR targeting. CellREADR mNeon distribution (green, left) and protein expression of target (purple, middle) are depicted at DIV 7. The fluorescence intensity profile to the left of each image set reveals the distribution of cells targeted by the CellREADR. Dashed red boxes indicate areas depicted in 1F; pia and white matter (WM) are illustrated with dotted lines.

E) Localization of CellREADR-targeted cells. CellREADR mNeon fluorescence intensity profiles measured across the depth of the cortex (0% depth = pial surface, 100% depth = white matter boundary) in 6 slices from 3 subjects. *FOXP2*-mNeon was relatively uniform throughout cortical layers, while *CALB2*-mNeon was more restricted to outer cortical layers.

F) Immunohistochemical characterization of CellREADR specificity. Representative images showing colocalization of CellREADR-mNeon with the corresponding target.

G) Quantification of CellREADR specificity, as measured by immunostaining. Each circular point denotes the specificity of labeling measured from an individual subject's tissue. Horizontal bars indicate mean specificity values for the CellREADRs. Throughout figures, data are presented as mean ± SEM.

H) Benchmarking of CellREADR efficiency with a human interneuron enhancer virus, DLX2.0-YFP. *CALB2* CellREADR and DLX2.0-YFP viruses (rAAV2-retro) were applied to slices cut sequentially from the same neocortical tissue specimen. Tissue was fixed 7 days after virus application, and immunostained against mNeon and YFP. Slice boundaries are indicated by the solid white line, and the white matter is demarcated by a dashed white line; colored boxes mark the inset images below.

I) Localization of DLX2.0-YFP expression. Representative image illustrating the efficiency and distribution of cellular labeling achieved with a DLX2.0-YFP virus (left), with fluorescence intensity profile (right) illustrating distribution of cells labeled by the virus. As compared to *CALB2* CellREADR labeling (Figures 1D and 1H), DLX2.0-YFP+ cells were less concentrated in the outer cortex, as would be expected for pan-interneuron targeting by DLX2.0.

J) Ability of DLX2.0-YFP to label the CALB2+ population. Quantification of colocalization of DLX2.0-YFP expression and CALB2, as measured by immunostaining (images not shown); note inter-subject variability in targeting of CALB2 cells.

K) Efficiency of *CALB2* CellREADR and DLX2.0-YFP viruses. Quantification of cells labeled per unit area. Note, although the CALB2 CellREADR is designed to target a subset of interneurons, rather than multiple classes of interneurons (as expected for DLX2.0), it actually labeled more cells, suggesting that it was more efficient.

Figure 2: PatchSeq validation of *CALB2* CellREADR targeting

A) Reference gene expression profiles of human MTG interneurons constructed by the Allen Institute[7]. *CALB2* expression is nearly restricted to *VIP* subclass interneurons, indicating that *CALB2* READR is expected to primarily target *VIP* interneurons. Of the 19 *CALB2* READR-targeted cells studied by PatchSeq in the current study, all but 1 cell mapped transcriptomically to the *VIP* subclass (the transcriptomic types of the 19 cells are listed at right, according to the classification scheme adapted from Tasic et al.[79] and Hodge et al.[7].

B) Expression of selected genes in *CALB2* READR cells. *CALB2* transcripts were detected in all but 1 cell, which was mapped onto the *SST* subclass (*SST KLDHC8A*). READR-targeted cells rarely expressed canonical markers of interneuron subclasses other than *VIP* (e.g., *LAMP5, SST, PVALB*). Interestingly, 5 of the 6 cells that mapped to the *PAX6 SYT6* type expressed the *SLC17A*7 (vesicular glutamate transporter 1), which is expressed widely across human MTG glutamatergic populations (Supplemental Figure 2); these cells also expressed the GABAergic marker, *GAD1*.

C) PatchSeq electrophysiological measures of *CALB2* READR-targeted neurons. Input-output curves illustrate the variation in rheobase, gain, and maximum firing frequency across the sampled population.

D) Variation in electrophysiological properties across and within interneuron transcriptomic types. Membrane responses to depolarizing and hyperpolarizing currents from cells that were mapped to the same transcriptomic types. Cells that mapped to the *PAX6 SYT6* type exhibited variation in the frequency and accommodation of action potential firing, and also exhibited varying responses to hyperpolarization.

E) Morphologies of *CALB2* READR-targeted cells. The positions (within cortical mantle) of reconstructed neurons are illustrated at top. The blue circles indicate the locations of the cell somata (not to scale), black profiles indicate the vertical and horizontal densities of cell dendrites, and red profiles indicate the vertical and horizontal densities of cell axons. Cortical depth is indicated on the left vertical axis; average cortical layer boundaries are shown on the right vertical axis. Complete cell tracings are shown at bottom.

Figure 3: *CALB2*- and *FOXP2-targeted* neurons exhibit distinct physiological profiles and spontaneous activities

A) Passive membrane properties of cells targeted by *CALB2* and *FOXP2* CellREADRs. Membrane capacitance and input resistance, but not hyperpolarizing sag ratio or resting membrane potential, differed statistically between the two target populations. Throughout this figure, black bars indicate mean and SEM.

B) Active properties of cells targeted by *CALB2* and *FOXP2* CellREADRs. Firing responses of cells in response to current injections, with frequency plotted against current step. Insets show action potentials elicited by current injections at twice cellular rheobase; these examples were selected to represent the mean input-output curves for each cell type. The rheobase (current that initiated firing), gain (initial slope), and max firing frequency all differed statistically between *CALB2* and *FOXP2* target populations.

C) Action potential(AP) properties of cells targeted by *CALB2* and *FOXP2* CellREADRs. Action potential half-width was measured at 50% of peak voltage (height), and was found to be smaller in *CALB2*-targeted cells. Action potential height and threshold did not vary between target cell groups. The fast afterhyperpolarization (fAHP) following the AP was larger in *CALB2*-targeted cells. Action potentials were aligned on their rising phase to compare AP waveforms between target cell groups. Group means are illustrated by the black lines. *CALB2*-targeted cells exhibited a shorter AP duration and a smaller afterdepolarization than the *FOXP2* population.

D) Subthreshold synaptic activity and suprathreshold firing were observed in targeted cells (held at resting membrane potential by current clamp with 0 pA current). Excitatory and inhibitory postsynaptic potentials (EPSPs and IPSPs, respectively) were detected in both *CALB2*- and *FOXP2*-targeted populations. Representative traces demonstrating EPSPs and IPSPs in cells of both populations are shown.

E) Recorded cells exhibited spontaneous firing from their resting potentials. Examples of spontaneous firing activity observed in 3 *CALB2*- (red) and 3 *FOXP2*-targeted cells (blue) are illustrated, with average firing frequencies (observed over a 3-minute period) indicated to the right of the traces.

F) *CALB2*-targeted cells were more likely than *FOXP2*-targeted cells to exhibit spontaneous firing in the slice preparation.

G) Spontaneous activity, measured as the frequency of spontaneous action potential firing, differed between *CALB2- and FOXP2*-targeted populations.

Figure 4: Cell type-specific optical manipulation of human neurons with CellREADR

A) CellREADR expression of an optogenetic effector, ChIEF, enables optogenetic control of action potential firing in *CALB2*- but not *FOXP2*-targeted cells. *CALB2*-ChIEF neurons fired action potentials in response to 100ms long, 642nm light pulses (left) or trains of 2ms pulses (6 of 6 cells fired action potentials in response to both stimuli). *FOXP2*-ChIEF neurons were depolarized, but they did not fire action potentials, in response to light stimuli (0 of 10 cells fired action potentials in response to stimuli).

B) Representative targeting scheme for optical interrogation of *CALB2* neuronal projections. Putative postsynaptic cells were labeled with a DLX2.0-YFP virus (left, green) and a binary CellREADR vector driving *CALB2*-ChIEF-tdTomato was used to manipulate presynaptic cells (middle, red). During optical stimulation of the ChIEF-tdTomato+ population, patch clamp recordings were made from YFP+/ChIEF-tdTomato- cells; at the end of recordings, biocytin-filled patched cells were recovered (right, purple).

C) Post-synaptic currents elicited by CALB2-ChIEF activation. Top, representative voltage clamp recordings made from a DLX2.0-YFP+/ChIEF-tdTomato- during optical stimulation of the CALB2-ChIEF population. Stimulation elicited optical post-synaptic currents (oPSCs), which were present at the glutamate reversal potential ($V_{rev(Glu)}$) but absent at the GABA reversal potential ($V_{rev(GABA)}$), indicating that they were mediated by synaptically released GABA. In DLX2.0-YFP+/ChIEF-tdTomato- cells, oPSCs were not observed at $V_{rev(GABA)}$. Bottom, recordings made from a hSyn-mCherry+ pyramidal neuron during optical stimulation of the *CALB2*-ChIEF population. In this recorded cell oPSCs were detected at $V_{rev(GABA)}$ but not $V_{rev(Glu)}$, indicating that it received GABAergic inputs from *CALB2*-ChIEF cells. In some other hSyn-tdTomato+ pyramidal cells, we detected oPSCs at $V_{rev(Glu)}$ but not $V_{rev(GABA)}$. No recorded cell exhibited oPSCs at both reversal potentials.

D) Waveforms of optically-evoked postsynaptic responses. Optical PSCs measured at $V_{rev(Glu)}$ from DLX2.0-YFP+/ChIEF-tdTomato- interneurons and hSyn-mCherry+ pyramidal neurons were normalized to the peak current. The monophasic rise time and small jitter relative to the 2ms light stimulus indicate that PSCs were monosynaptic events directly triggered by the optical pulse.

E) Quantification of postsynaptic cell responses to *CALB2*-ChIEF activation. Recordings were made from 12 DLX2.0-YFP+/*CALB2*-ChIEF- interneurons during *CALB2*-ChIEF activation. Optical inhibitory PSCs (oIPSCs, oPSCs detected at $V_{rev(Glu)}$) were observed in 4 of 12 cells (33.3%), and optical excitatory PSCs (oEPSCs, oPSCs detected at $V_{rev(GABA)}$) were not detected. Recordings were also made from 12 hSyn-tdTomato+ pyramidal neurons during *CALB2*-ChIEF activation. Optical IPSCs were detected in 2 of 12 cells (16.7%), and oEPSCs were detected in 2 of 12 cells (16.7%).

Figure 5: Cell type-specific monitoring of population activity with CellREADR

A) Correlation between action potential firing and GCamp7f signals. Action potentials (black) were elicited by current injections in single cells expressing either *CALB2*-GCamp7f or *FOXP2*-GCamp7f (top left; current injection is represented by gray box; the upper inset shows the voltage trace at an expanded time scale to show the individual action potentials). Calcium transients (green, bottom left) were concurrently imaged at the cell soma and proximal dendritic compartment. Traces show 6 action potentials and resultant GCaMP ΔF/F signal measured from a *CALB2*-GCamp7f cell. The relationship between the baseline-subtracted change in fluorescence and action potential firing (right) was established by varying the current injection, counting action potentials, and fitting the ΔF/F to action potential counts with a linear function (*CALB2*: $R^2 = 0.84$; *FOXP2*: $R^2 = 0.93$).

B) Calcium imaging detects subthreshold events as well as action potentials. Recording of a *CALB2*-GCaMP7f demonstrating three evoked action potentials (black trace, at grey box) followed by a spontaneous subthreshold depolarization that was followed by a single spontaneous action potential. The calcium transient for these three events (green) is depicted; the rise times for each event were as follows: τ_{3AP} = 390ms, $\tau_{Depolarization}$ = 1760ms, τ_{1AP} = 202ms.

C) Population activities of *CALB2*-GCamp7f (left, red) and *FOXP2*-GCamp7f (right, blue) neurons measured in baseline conditions (standard artificial cerebrospinal fluid). Background-subtracted fluorescent profiles of cell somata were collected from a maximum projection of 90s video stacks (red and blue traces). CellREADR typically labeled 10-50 cells within a field of view.

D) Color maps depicting population calcium signal dynamics. Calcium signals from *CALB2*-GCamp7f (left, red) or *FOXP2*-GCamp7f cells (right, blue) are represented by a color map (intensity scale at bottom). Each map represents a recording performed on a single slice; slices were derived from 4 subjects. Spontaneous activity levels varied between slices. Calcium signal traces from selected individual cells are depicted to the right of the color maps; most transients were small-amplitude, fast-rising events, similar to the transients produced by action potentials in (A). Large-amplitude, slow-rising transients (marked with asterisks) similar to the subthreshold events in (B), were also observed.

E) Correlated calcium events in slice populations. The correlation of cellular *CALB2*-GCaMP7f or *FOXP2*-GCaMP7f calcium signals was measured within each slice, and then compared between groups (*CALB2*- and *FOXP2*-targeted populations). Calcium signals were more strongly correlated in the *FOXP2*-targeted population.

F) Calcium signal responses to nicotinic acetylcholine receptor activation. Nicotine (300μM) was applied to a subset of slices following imaging of baseline activity. The number of active cells in the *CALB2*-GCaMP7f (left, red) and *FOXP2*-GCaMP7f populations did not statistically differ between baseline and treatment conditions (nicotine application); the *CALB2*-GCaMP7f

population exhibited a non-significant trend towards increased activity (*CALB2* p=0.09, *FOXP2* p=0.999 by Fisher exact test).

Table 1: Patient demographics and specimen utilization

Patient ID	Age	Sex	Region	Where data was contributed
TE22	8	M	R parietal neocortex	*FOXP2* physiology
TE23	60	M	L temporal neocortex	*FOXP2* physiology
TE29	43	M	L temporal neocortex	*CALB2* physiology & morphology
TE30	52	M	R temporal neocortex	*CALB2* morphology
TE31	28	M	R temporal neocortex	*CALB2* morphology
TE32	12	F	L temporal neocortex	*SST* expression
TE33	45	M	L temporal neocortex	*UNC5B* expression, *CALB2* physiology & morphology
TE34	19	F	R temporal neocortex	*CALB2* physiology & morphology
TE35	30	M	L temporal neocortex	*PVALB* expression
TE36	35	F	R temporal neocortex	*CALB2* expression
TE37	23	M	R temporal neocortex	*CALB2* physiology
TE41	42	M	R temporal neocortex	*CALB2* physiology
TE44	14	M	L temporal neocortex	*CALB2* physiology
TE45	41	M	L temporal neocortex	*CALB2* physiology
TE46	43	F	L temporal neocortex	*CALB2* physiology
TE47	28	F	L temporal neocortex	*FOXP2* expression & physiology, Calcium imaging
TE48	40	F	R temporal neocortex	*FOXP2* physiology
TE50	35	F	R temporal neocortex	*FOXP2* physiology, Calcium imaging
TE51	29	F	R temporal neocortex	*FOXP2* physiology
TE52	19	M	L temporal neocortex	*FOXP2* physiology, Calcium imaging
TE53	33	M	R temporal neocortex	*FOXP2* physiology, Calcium imaging
TE57	34	F	L temporal neocortex	Calcium imaging

Supplemental Figure Legends

Supplemental Figure 1: Correlation between expression of specific genes and physiological characteristics of PatchSeq cells

A) RNA expression counts for the BK channel alpha (*KCNMA1*) and beta subunits (*KCNMB1-4*) are shown for each cell that completed PatchSeq, and the cells are sorted from left-to-right by decreasing amplitude of the fast afterhyperpolarization (fAHP) following single action potentials. As expected, the average expression of all BK channel subunits correlates with fAHP amplitude, especially with the pore-forming alpha subunit. The plot at right shows the relationship between average BK channel expression and the fAHP amplitude (R^2 = 0.19).

B) RNA expression counts for the BK channel subunits but sorted from left-to-right by increasing action potential duration. As for the fAHP, the expression of BK channel subunits correlates with the AP duration. Plot at right shows the relationship between average BK channel expression and the AP duration (R^2 = 0.17).

Supplemental Figure 2: Human MTG transcriptomic data referenced in current study.

A) Reference gene expression profiles of human MTG neurons constructed by the Allen Institute[59]. FOXP2 expression is nearly restricted to the excitatory neuron class and expressed widely across excitatory neuron types.

B) Illustration of restricted cellular targeting achieved by CellREADR. Counts of interneuron transcriptomic types identified in a reference atlas obtained primarily with acute post-mortem tissues (left column, human MTG)[59]. Transcriptomic types characterized in a BICCN supported PatchSeq study, which utilized the DLX2.0 enhancer virus to target the interneuron class (in addition to patching of unlabeled cells; middle)[42]. Counts of CALB2 READR-targeted cells that were assessed by RNAseq in the current pilot study; note utility of CellREADR for systematic access to specific populations.

Acknowledgements

This study was supported in part by NIH grants 1DP1MH129954-01 (Z.J.H.), 1DP2MH140149 (D.G.S.), and 1K08NS133292 (J.B.R). J.B.R. was supported by the NINDS K12 Child Neurologist Career Development Program. D.G.S was supported by the NINDS K12 Neurosurgery Research Career Development Program, The Klingenstein-Simons Fellowship Award in Neuroscience, The Whitehall Foundation, and the Ruth K. Broad Foundation for Biomedical Research. The content is solely the responsibility of the authors and does not necessarily represent the official views of the National Institutes of Health. We thank the Duke Light Microscopy Core Facility and the Duke Sequencing and Genomics Core for their support in data acquisition and analysis. We are grateful to the human subjects who donated surgical tissue specimens for this research.

Author Contributions

Concept and methodology: E.A.M., J.B.R., Y.Q., J.Z.H., D.G.S.,
Data acquisition and analysis: E.A.M., J.B.R., S.Z., P.T., M.M.
Resources: M.L.V., D.G.S. (surgical tissue specimens); Y.Q., S.Z., Z.J.H. (CellREADR viruses)
Writing: E.A.M., J.B.R., Z.J.H., D.G.S.
Funding: Z.J.H., D.G.S.

Declaration of Interests

Z.J.H. has filed patents for CellREADR (US patent #: PCT/US22/79004 & PCT/US22/7900). Z.J.H is a co-founder of Doppler Bio. All other authors have no conflicts of interest to declare.

References

1. Zeng, H. & Sanes, J. R. Neuronal cell-type classification: challenges, opportunities and the path forward. *Nat. Rev. Neurosci.* **18**, 530–546 (2017).
2. Konopka, G. & Bhaduri, A. Functional genomics and systems biology in human neuroscience. *Nature* **623**, 274–282 (2023).
3. Jorstad, N. L. *et al.* Comparative transcriptomics reveals human-specific cortical features. *Science* **382**, eade9516 (2023).
4. Siletti, K. *et al.* Transcriptomic diversity of cell types across the adult human brain. *Science* **382**, eadd7046 (2023).
5. Jorstad, N. L. *et al.* Transcriptomic cytoarchitecture reveals principles of human neocortex

organization. *Science* **382**, eadf6812 (2023).

6. Bakken, T. E. *et al.* Comparative cellular analysis of motor cortex in human, marmoset and mouse. *Nature* **598**, 111–119 (2021).
7. Hodge, R. D. *et al.* Conserved cell types with divergent features in human versus mouse cortex. *Nature* **573**, 61–68 (2019).
8. Hawrylycz, M. J. *et al.* An anatomically comprehensive atlas of the adult human brain transcriptome. *Nature* **489**, 391–399 (2012).
9. Krienen, F. M. *et al.* Innovations present in the primate interneuron repertoire. *Nature* **586**, 262–269 (2020).
10. Yao, Z. *et al.* A high-resolution transcriptomic and spatial atlas of cell types in the whole mouse brain. *Nature* **624**, 317–332 (2023).
11. BRAIN Initiative Cell Census Network (BICCN). A multimodal cell census and atlas of the mammalian primary motor cortex. *Nature* **598**, 86–102 (2021).
12. Tasic, B. *et al.* Adult mouse cortical cell taxonomy revealed by single cell transcriptomics. *Nat. Neurosci.* **19**, 335–346 (2016).
13. Shi, Y. *et al.* Mouse and human share conserved transcriptional programs for interneuron development. *Science* **374**, eabj6641 (2021).
14. Lee, A. T., Chang, E. F., Paredes, M. F. & Nowakowski, T. J. Large-scale neurophysiology and single-cell profiling in human neuroscience. *Nature* **630**, 587–595 (2024).
15. He, M. & Huang, Z. J. Genetic approaches to access cell types in mammalian nervous systems. *Curr. Opin. Neurobiol.* **50**, 109–118 (2018).
16. Feng, G. *et al.* Opportunities and limitations of genetically modified nonhuman primate models for neuroscience research. *Proc. Natl. Acad. Sci. U. S. A.* **117**, 24022–24031 (2020).
17. Taniguchi, H. *et al.* A resource of Cre driver lines for genetic targeting of GABAergic neurons in cerebral cortex. *Neuron* **71**, 995–1013 (2011).

18. Huang, Z. J. & Zeng, H. Genetic approaches to neural circuits in the mouse. *Annu. Rev. Neurosci.* **36**, 183–215 (2013).
19. Vormstein-Schneider, D. *et al.* Viral manipulation of functionally distinct interneurons in mice, non-human primates and humans. *Nat. Neurosci.* **23**, 1629–1636 (2020).
20. Mich, J. K. *et al.* Functional enhancer elements drive subclass-selective expression from mouse to primate neocortex. *Cell Rep.* **34**, 108754 (2021).
21. Graybuck, L. T. *et al.* Enhancer viruses for combinatorial cell-subclass-specific labeling. *Neuron* **109**, 1449–1464.e13 (2021).
22. Dimidschstein, J. *et al.* A viral strategy for targeting and manipulating interneurons across vertebrate species. *Nat. Neurosci.* **19**, 1743–1749 (2016).
23. Heinz, S., Romanoski, C. E., Benner, C. & Glass, C. K. The selection and function of cell type-specific enhancers. *Nat. Rev. Mol. Cell Biol.* **16**, 144–154 (2015).
24. Hardison, R. C. & Taylor, J. Genomic approaches towards finding cis-regulatory modules in animals. *Nat. Rev. Genet.* **13**, 469–483 (2012).
25. Challis, R. C. *et al.* Adeno-Associated Virus Toolkit to Target Diverse Brain Cells. *Annu. Rev. Neurosci.* **45**, 447–469 (2022).
26. Hoffmann, M. D., Gallant, J. P., LeBeau, A. M. & Schmidt, D. Unlocking precision gene therapy: harnessing AAV tropism with nanobody swapping at capsid hotspots. *NAR Mol Med* **1**, ugae008 (2024).
27. Castle, M. J., Turunen, H. T., Vandenberghe, L. H. & Wolfe, J. H. Controlling AAV tropism in the nervous system with natural and engineered capsids. *Methods Mol. Biol.* **1382**, 133–149 (2016).
28. Matsuzaki, Y., Fukai, Y., Konno, A. & Hirai, H. Optimal AAV capsid/promoter combinations to target specific cell types in the common marmoset cerebral cortex. *bioRxiv* (2024) doi:10.1101/2024.05.09.593444.
29. Sun, S. & Schaffer, D. V. Engineered viral vectors for functional interrogation,

deconvolution, and manipulation of neural circuits. *Curr. Opin. Neurobiol.* **50**, 163–170 (2018).

30. Campos, L. J. *et al.* Advances in AAV technology for delivering genetically encoded cargo to the nonhuman primate nervous system. *Curr. Res. Neurobiol.* **4**, 100086 (2023).
31. Eugène, E. *et al.* An organotypic brain slice preparation from adult patients with temporal lobe epilepsy. *J. Neurosci. Methods* **235**, 234–244 (2014).
32. Schwarz, N. *et al.* Long-term adult human brain slice cultures as a model system to study human CNS circuitry and disease. *Elife* **8**, (2019).
33. Cohen, I., Navarro, V., Clemenceau, S., Baulac, M. & Miles, R. On the origin of interictal activity in human temporal lobe epilepsy in vitro. *Science* **298**, 1418–1421 (2002).
34. Gonzalez-Ramos, A. *et al.* Human stem cell-derived GABAergic neurons functionally integrate into human neuronal networks. *Sci. Rep.* **11**, 22050 (2021).
35. Dossi, E. *et al.* Pannexin-1 channels contribute to seizure generation in human epileptic brain tissue and in a mouse model of epilepsy. *Sci. Transl. Med.* **10**, (2018).
36. Andersson, M. *et al.* Optogenetic control of human neurons in organotypic brain cultures. *Sci. Rep.* **6**, 24818 (2016).
37. Kalmbach, B. E. *et al.* h-Channels Contribute to Divergent Intrinsic Membrane Properties of Supragranular Pyramidal Neurons in Human versus Mouse Cerebral Cortex. *Neuron* **100**, 1194–1208.e5 (2018).
38. Ting, J. T. *et al.* A robust ex vivo experimental platform for molecular-genetic dissection of adult human neocortical cell types and circuits. *Sci. Rep.* **8**, 8407 (2018).
39. Beaulieu-Laroche, L. *et al.* Allometric rules for mammalian cortical layer 5 neuron biophysics. *Nature* **600**, 274–278 (2021).
40. Moradi Chameh, H. *et al.* Diversity amongst human cortical pyramidal neurons revealed via their sag currents and frequency preferences. *Nat. Commun.* **12**, 2497 (2021).
41. Wilbers, R. *et al.* Structural and functional specializations of human fast-spiking neurons

support fast cortical signaling. *Sci. Adv.* **9**, eadf0708 (2023).

42. Lee, B. R. *et al.* Signature morphoelectric properties of diverse GABAergic interneurons in the human neocortex. *Science* **382**, eadf6484 (2023).
43. Chartrand, T. *et al.* Morphoelectric and transcriptomic divergence of the layer 1 interneuron repertoire in human versus mouse neocortex. *Science* **382**, eadf0805 (2023).
44. Berg, J. *et al.* Human neocortical expansion involves glutamatergic neuron diversification. *Nature* **598**, 151–158 (2021).
45. Buchin, A. *et al.* Multi-modal characterization and simulation of human epileptic circuitry. *Cell Rep.* **41**, 111873 (2022).
46. Boldog, E. *et al.* Transcriptomic and morphophysiological evidence for a specialized human cortical GABAergic cell type. *Nat. Neurosci.* **21**, 1185–1195 (2018).
47. Oláh, S. *et al.* Output of neurogliaform cells to various neuron types in the human and rat cerebral cortex. *Front. Neural Circuits* **1**, 4 (2007).
48. Qian, Y. *et al.* Programmable RNA sensing for cell monitoring and manipulation. *Nature* **610**, 713–721 (2022).
49. Jiang, K. *et al.* Programmable eukaryotic protein synthesis with RNA sensors by harnessing ADAR. *Nat. Biotechnol.* **41**, 698–707 (2023).
50. Kaseniit, K. E. *et al.* Modular, programmable RNA sensing using ADAR editing in living cells. *Nat. Biotechnol.* **41**, 482–487 (2023).
51. MacDermot, K. D. *et al.* Identification of FOXP2 truncation as a novel cause of developmental speech and language deficits. *Am. J. Hum. Genet.* **76**, 1074–1080 (2005).
52. Lai, C. S., Fisher, S. E., Hurst, J. A., Vargha-Khadem, F. & Monaco, A. P. A forkhead-domain gene is mutated in a severe speech and language disorder. *Nature* **413**, 519–523 (2001).
53. Haesler, S. *et al.* Incomplete and inaccurate vocal imitation after knockdown of FoxP2 in songbird basal ganglia nucleus Area X. *PLoS Biol.* **5**, e321 (2007).

54. Groszer, M. *et al.* Impaired synaptic plasticity and motor learning in mice with a point mutation implicated in human speech deficits. *Curr. Biol.* **18**, 354–362 (2008).
55. Ferland, R. J., Cherry, T. J., Preware, P. O., Morrisey, E. E. & Walsh, C. A. Characterization of Foxp2 and Foxp1 mRNA and protein in the developing and mature brain. *J. Comp. Neurol.* **460**, 266–279 (2003).
56. Allen Brain Atlas - ISH Data - Cortex Study.
57. Medalla, M. *et al.* Comparative features of calretinin, calbindin, and parvalbumin expressing interneurons in mouse and monkey primary visual and frontal cortices. *J. Comp. Neurol.* **531**, 1934–1962 (2023).
58. Guet-McCreight, A., Skinner, F. K. & Topolnik, L. Common Principles in Functional Organization of VIP/Calretinin Cell-Driven Disinhibitory Circuits Across Cortical Areas. *Front. Neural Circuits* **14**, 32 (2020).
59. Allen Brain Atlas - Cell Types - Human MTG.
60. Džaja, D., Hladnik, A., Bičanić, I., Baković, M. & Petanjek, Z. Neocortical calretinin neurons in primates: increase in proportion and microcircuitry structure. *Front. Neuroanat.* **8**, 103 (2014).
61. Hladnik, A., Džaja, D., Darmopil, S., Jovanov-Milošević, N. & Petanjek, Z. Spatio-temporal extension in site of origin for cortical calretinin neurons in primates. *Front. Neuroanat.* **8**, 50 (2014).
62. *Scrattch: Single Cell RNA-Seq Analysis for Transcriptomic Type Characterization*. (Github).
63. Allen Brain Map. *Documentation: Cell Types Database* https://community.brain-map.org/t/documentation-cell-types-database/2845.
64. Shao, L. R., Halvorsrud, R., Borg-Graham, L. & Storm, J. F. The role of BK-type Ca2+-dependent K+ channels in spike broadening during repetitive firing in rat hippocampal pyramidal cells. *J. Physiol.* **521 Pt 1**, 135–146 (1999).
65. Lancaster, B. & Nicoll, R. A. Properties of two calcium-activated hyperpolarizations in rat

hippocampal neurones. *J. Physiol.* **389**, 187–203 (1987).

66. Gouwens, N. W. *et al.* Classification of electrophysiological and morphological neuron types in the mouse visual cortex. *Nat. Neurosci.* **22**, 1182–1195 (2019).
67. Jonas, P., Bischofberger, J., Fricker, D. & Miles, R. Interneuron Diversity series: Fast in, fast out--temporal and spatial signal processing in hippocampal interneurons. *Trends Neurosci.* **27**, 30–40 (2004).
68. Markram, H. *et al.* Interneurons of the neocortical inhibitory system. *Nat. Rev. Neurosci.* **5**, 793–807 (2004).
69. Lin, J. Y., Lin, M. Z., Steinbach, P. & Tsien, R. Y. Characterization of engineered channelrhodopsin variants with improved properties and kinetics. *Biophys. J.* **96**, 1803–1814 (2009).
70. Caputi, A., Rozov, A., Blatow, M. & Monyer, H. Two calretinin-positive GABAergic cell types in layer 2/3 of the mouse neocortex provide different forms of inhibition. *Cereb. Cortex* **19**, 1345–1359 (2009).
71. Gulyás, A. I., Hájos, N. & Freund, T. F. Interneurons containing calretinin are specialized to control other interneurons in the rat hippocampus. *J. Neurosci.* **16**, 3397–3411 (1996).
72. Meskenaite, V. Calretinin-immunoreactive local circuit neurons in area 17 of the cynomolgus monkey, Macaca fascicularis. *J. Comp. Neurol.* **379**, 113–132 (1997).
73. Paunovska, K., Loughrey, D. & Dahlman, J. E. Drug delivery systems for RNA therapeutics. *Nat. Rev. Genet.* **23**, 265–280 (2022).
74. Hou, X., Zaks, T., Langer, R. & Dong, Y. Lipid nanoparticles for mRNA delivery. *Nat Rev Mater* **6**, 1078–1094 (2021).
75. Kügler, S., Kilic, E. & Bähr, M. Human synapsin 1 gene promoter confers highly neuron-specific long-term transgene expression from an adenoviral vector in the adult rat brain depending on the transduced area. *Gene Ther.* **10**, 337–347 (2003).
76. Furlanis, E. *et al.* An enhancer-AAV toolbox to target and manipulate distinct interneuron

subtypes. *bioRxivorg* (2024) doi:10.1101/2024.07.17.603924.

77. Brian Lee, K. H. *Patch-Seq Recording and Extraction Detailed Protocol*. dx.doi.org/10.17504/protocols.io.bw6gphbw (2021) doi:10.17504/protocols.io.bw6gphbw.

78. Peng, H., Bria, A., Zhou, Z., Iannello, G. & Long, F. Extensible visualization and analysis for multidimensional images using Vaa3D. *Nat. Protoc.* **9**, 193–208 (2014).

79. Tasic, B. *et al.* Shared and distinct transcriptomic cell types across neocortical areas. *Nature* **563**, 72–78 (2018).

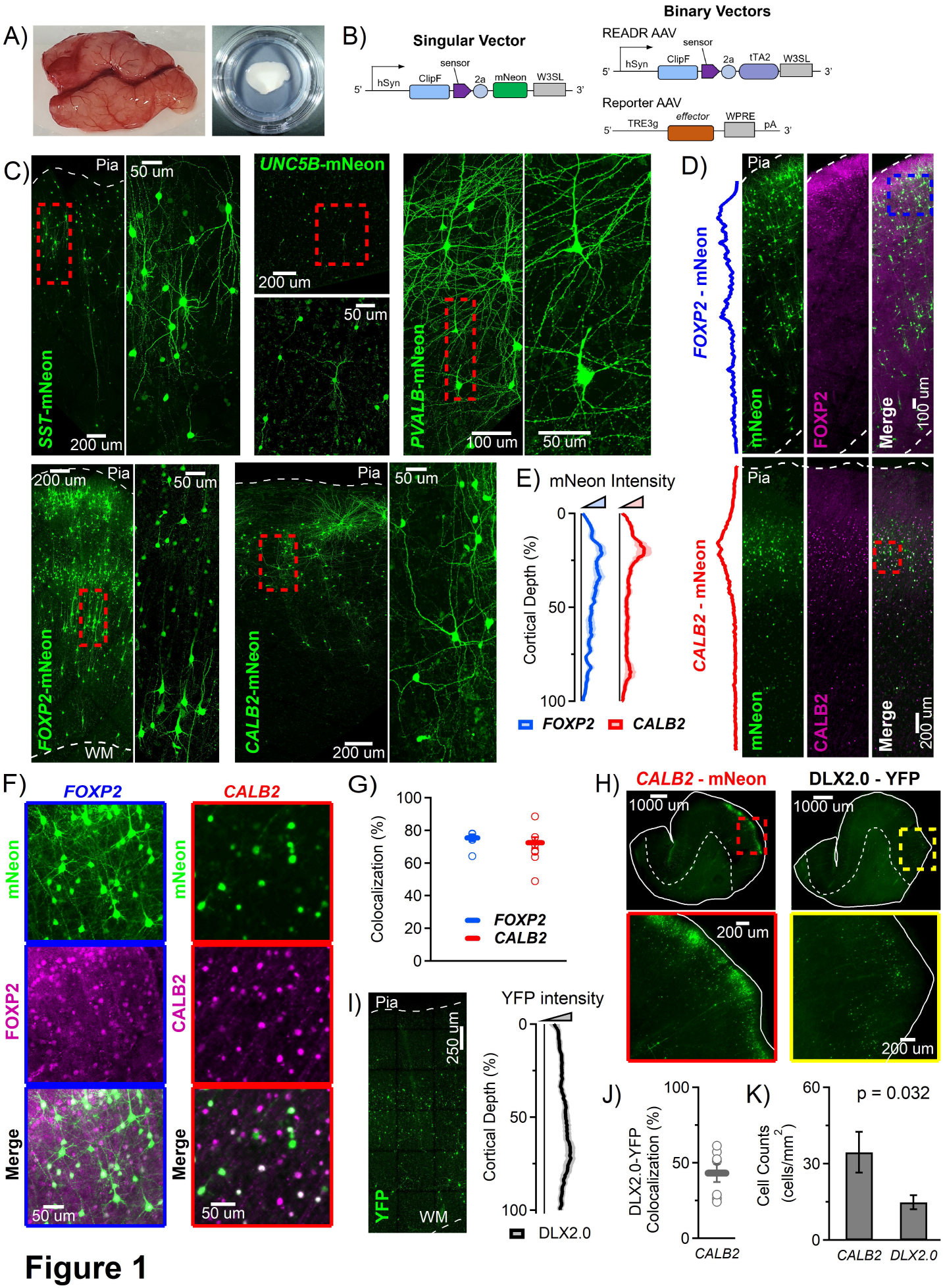

Figure 1

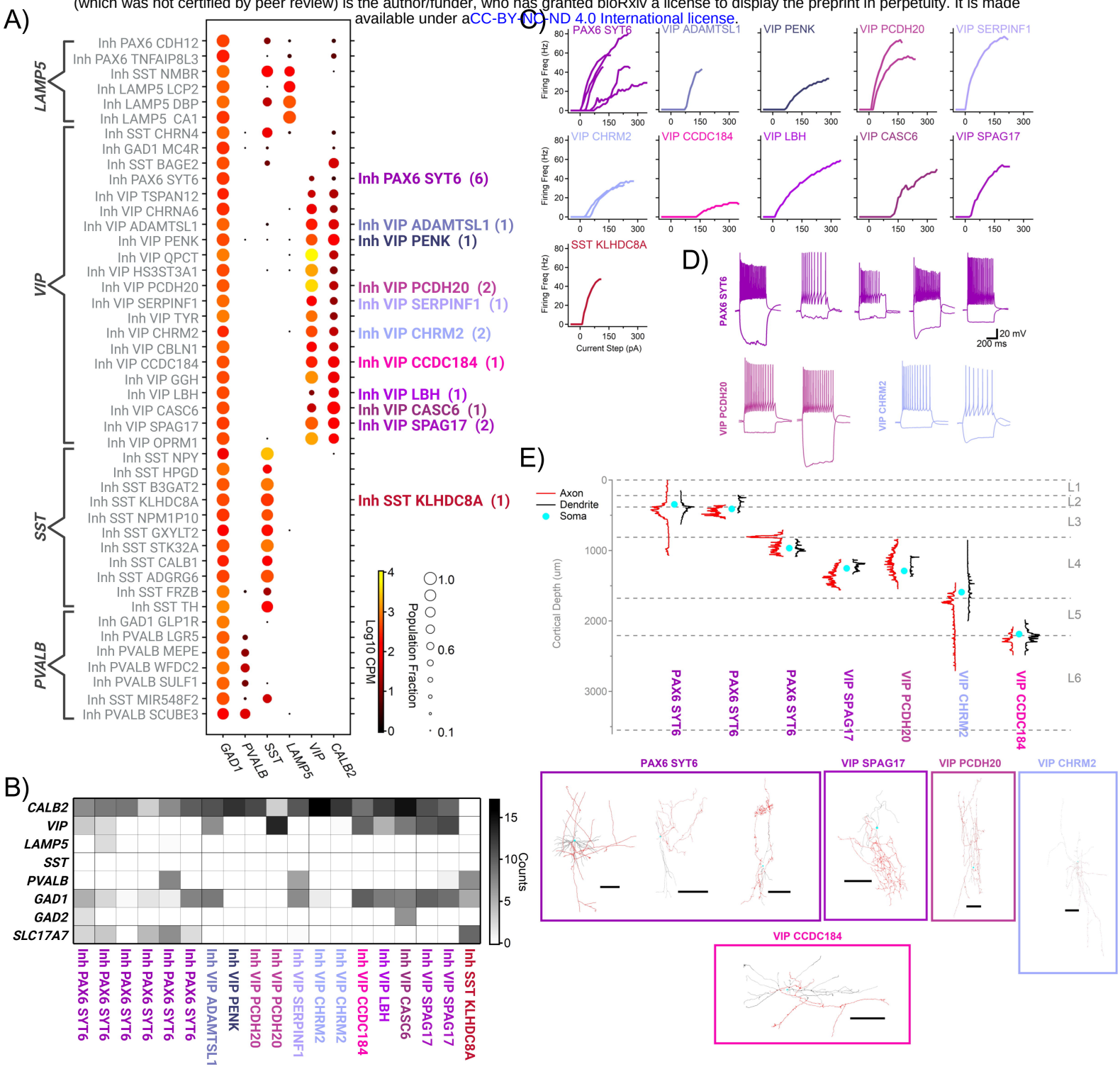

Figure 2

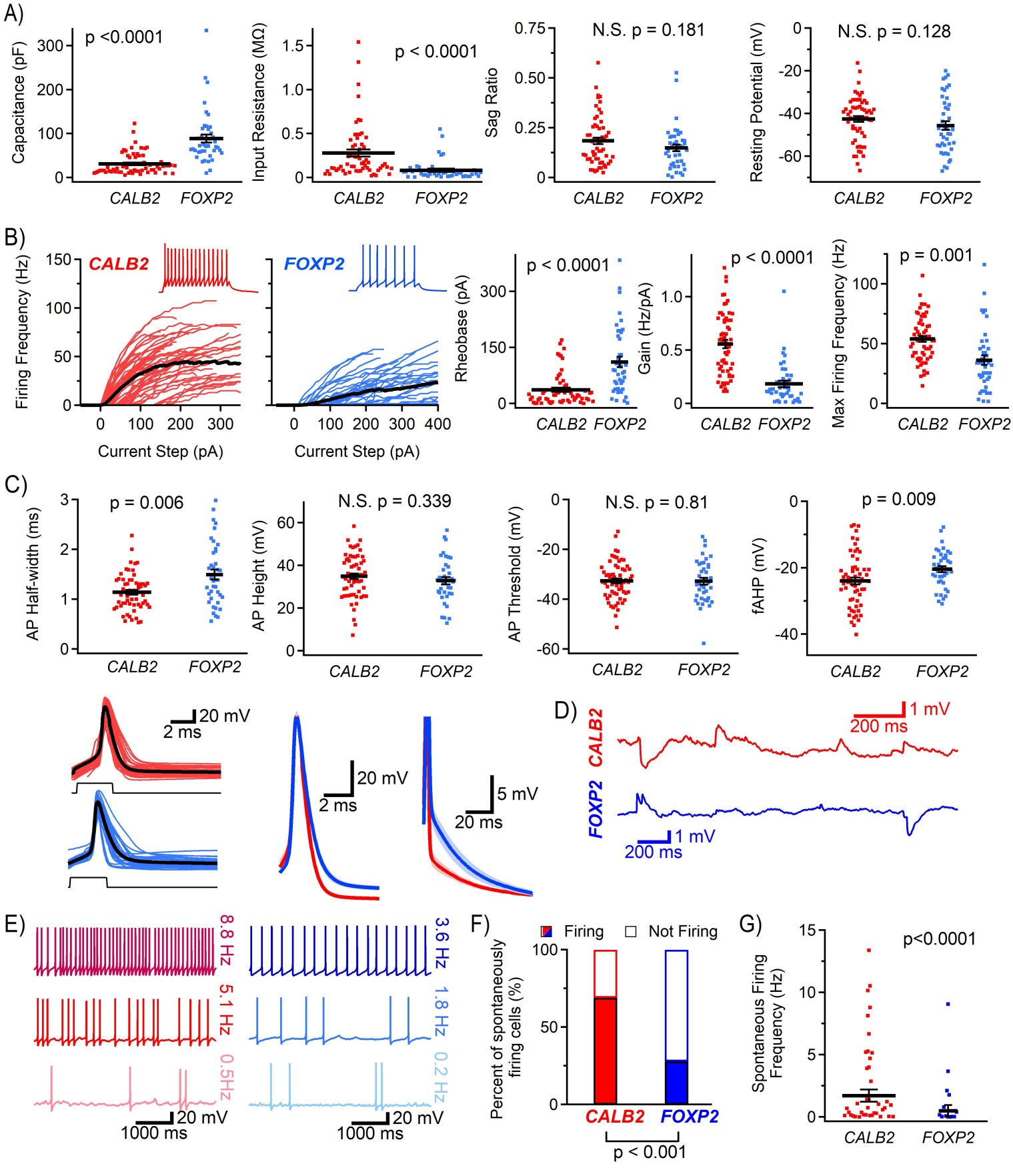
A)
Capacitance (pF)
p <0.0001
Input Resistance (MΩ)
p < 0.0001
Sag Ratio
N.S. p = 0.181
Resting Potential (mV)
N.S. p = 0.128
CALB2
FOXP2
B)
Firing Frequency (Hz)
CALB2
FOXP2
Current Step (pA)
Rheobase (pA)
p < 0.0001
Gain (Hz/pA)
p < 0.0001
Max Firing Frequency (Hz)
p = 0.001
C)
AP Half-width (ms)
p = 0.006
AP Height (mV)
N.S. p = 0.339
AP Threshold (mV)
N.S. p = 0.81
fAHP (mV)
p = 0.009
20 mV
2 ms
5 mV
20 ms
D)
1 mV
200 ms
E)
8.8 Hz
5.1 Hz
0.5Hz
3.6 Hz
1.8 Hz
0.2 Hz
1000 ms
F)
Firing
Not Firing
Percent of spontaneously firing cells (%)
p < 0.001
G)
Spontaneous Firing Frequency (Hz)
p<0.0001

Figure 3

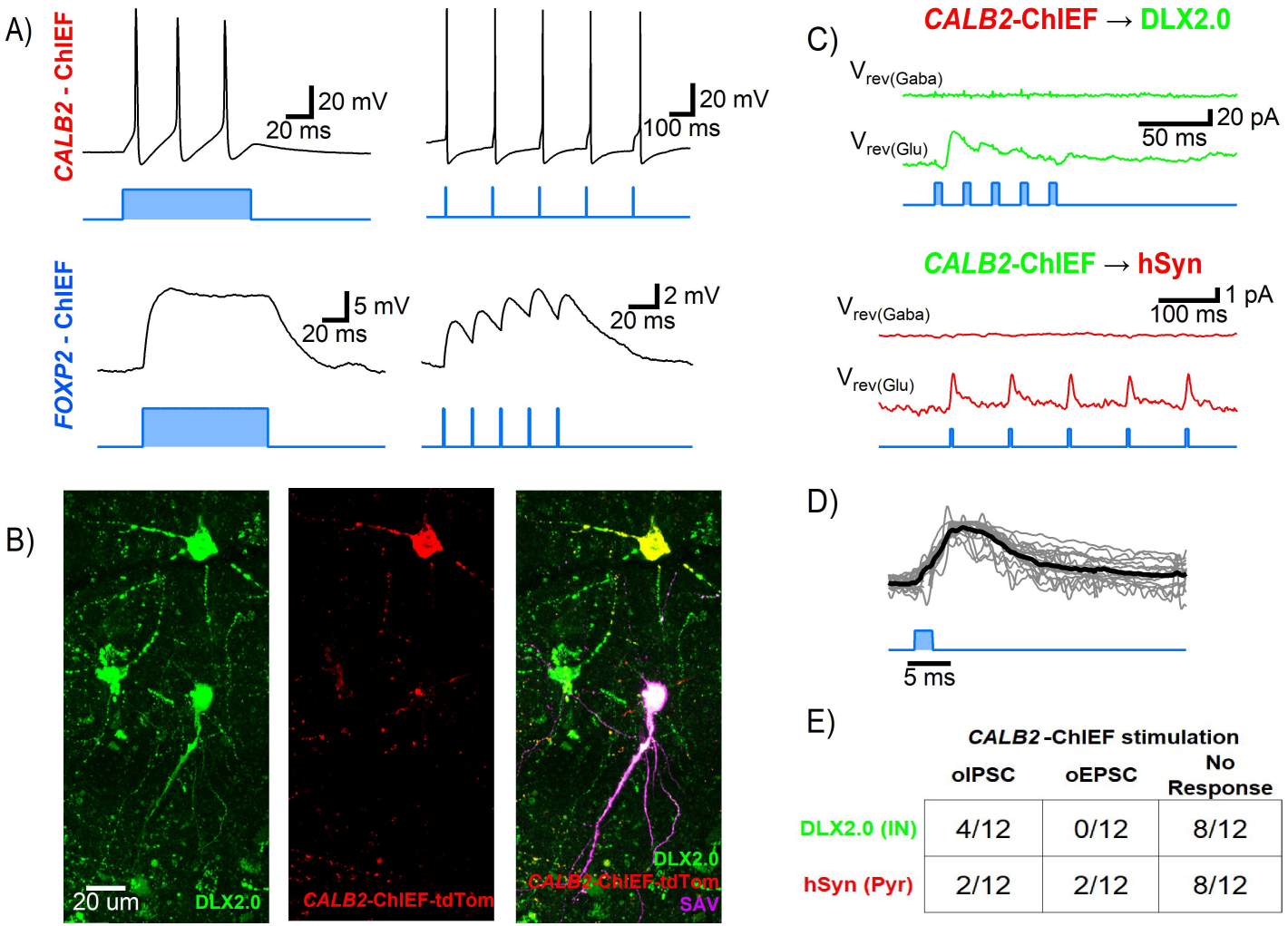

	oIPSC	oEPSC	No Response
DLX2.0 (IN)	4/12	0/12	8/12
hSyn (Pyr)	2/12	2/12	8/12

Figure 4

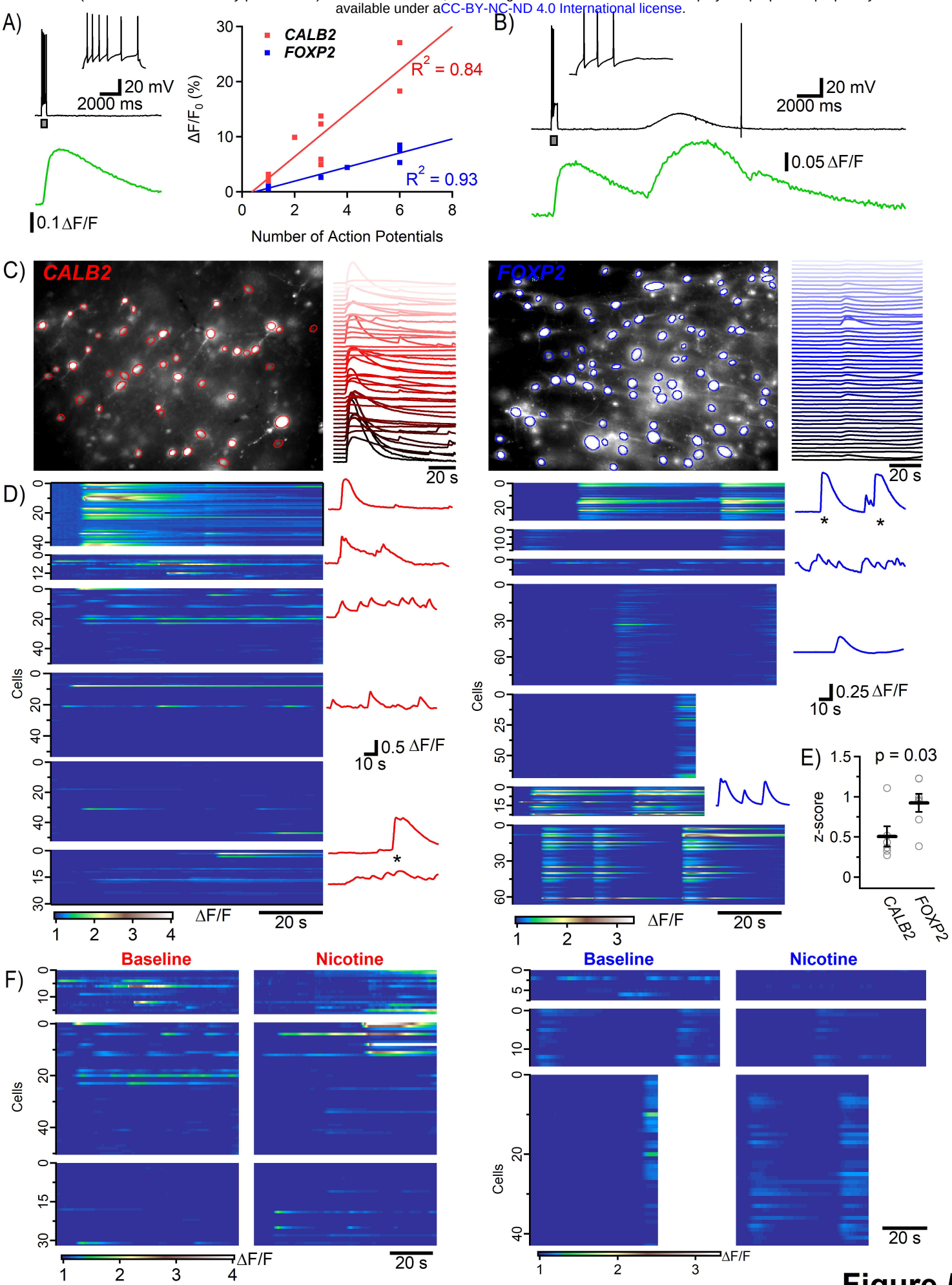

Figure 5

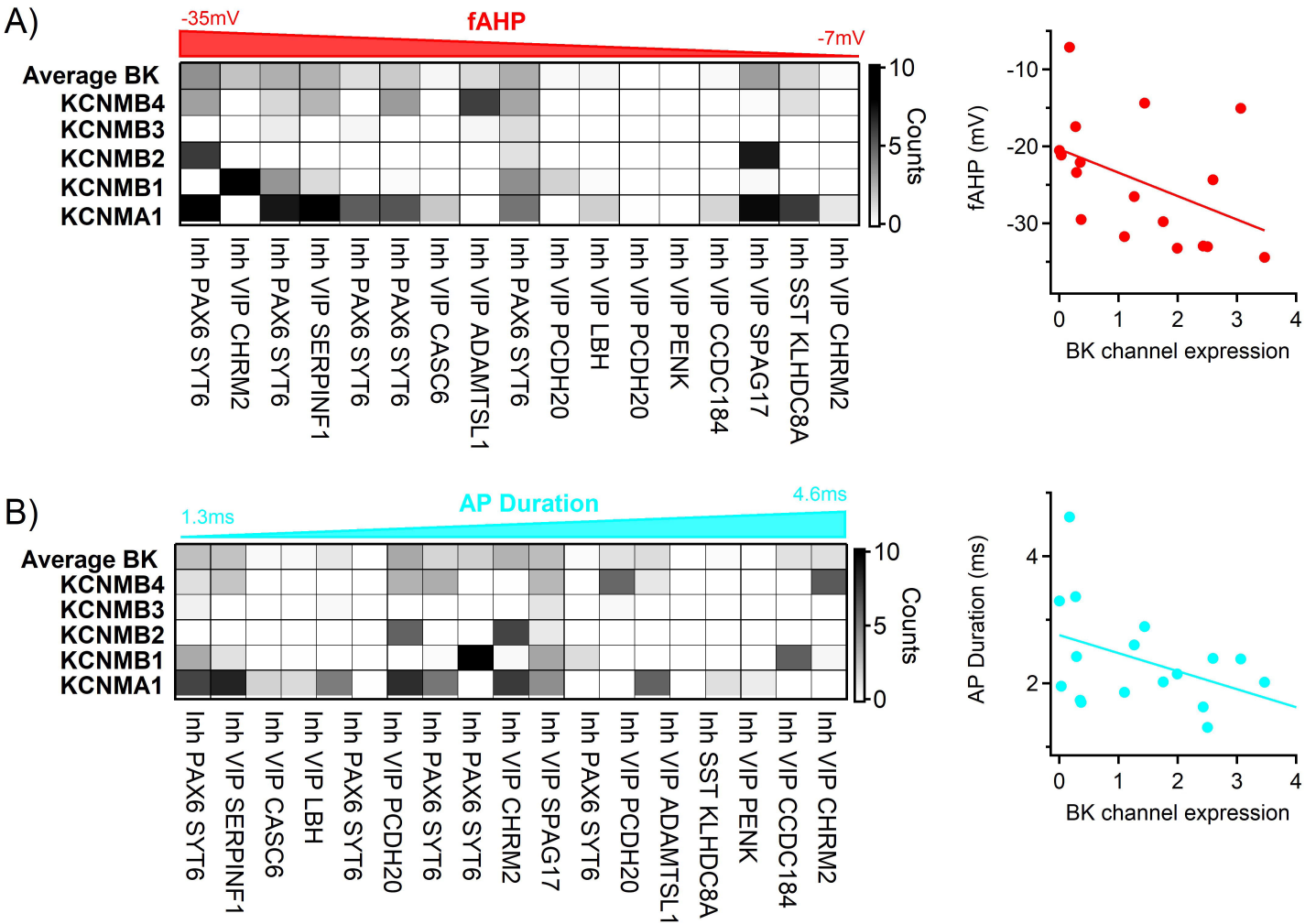
A)
-35mV
fAHP
-7mV
Average BK
KCNMB4
KCNMB3
KCNMB2
KCNMB1
KCNMA1
10
5
0
Counts
Inh PAX6 SYT6
Inh VIP CHRM2
Inh PAX6 SYT6
Inh VIP SERPINF1
Inh PAX6 SYT6
Inh PAX6 SYT6
Inh VIP CASC6
Inh VIP ADAMTSL1
Inh PAX6 SYT6
Inh VIP PCDH20
Inh VIP LBH
Inh VIP PCDH20
Inh VIP PENK
Inh VIP CCDC184
Inh VIP SPAG17
Inh SST KLHDC8A
Inh VIP CHRM2
fAHP (mV)
-10
-20
-30
0
1
2
3
4
BK channel expression
B)
1.3ms
AP Duration
4.6ms
Average BK
KCNMB4
KCNMB3
KCNMB2
KCNMB1
KCNMA1
10
5
0
Counts
Inh PAX6 SYT6
Inh VIP SERPINF1
Inh VIP CASC6
Inh VIP LBH
Inh PAX6 SYT6
Inh VIP PCDH20
Inh PAX6 SYT6
Inh PAX6 SYT6
Inh VIP CHRM2
Inh VIP SPAG17
Inh PAX6 SYT6
Inh VIP PCDH20
Inh VIP ADAMTSL1
Inh SST KLHDC8A
Inh VIP PENK
Inh VIP CCDC184
Inh VIP CHRM2
AP Duration (ms)
4
2
0
1
2
3
4
BK channel expression

Sup. Figure 1

A)

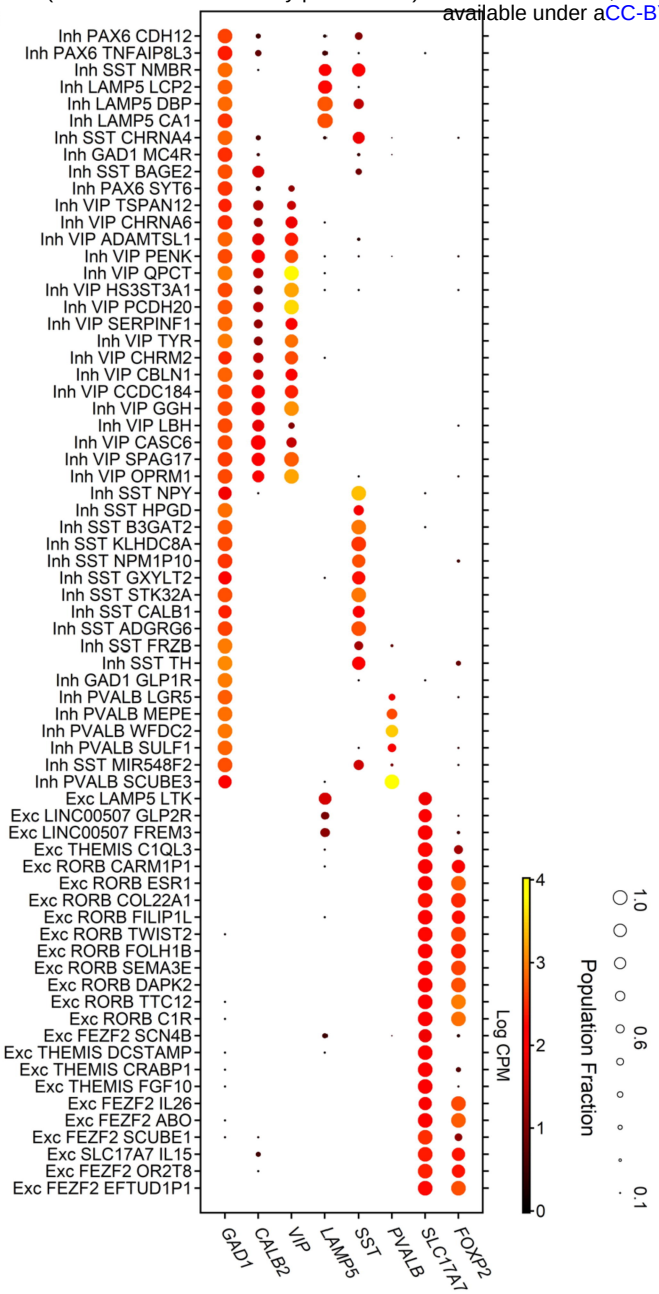

B)

		Count (human MTG)	Count (Lee, 2023)	Count
PVALB	Inh PVALB SCUBE3	47	11	
	Inh SST MIR548F2	80	27	
	Inh PVALB SULF1	167	30	
	Inh PVALB WFDC2	387	168	
	Inh PVALB MEPE	64	80	
	Inh PVALB LGR5	52	2	
	Inh GAD1 GLP1R	27	4	
SST	Inh SST TH	27	16	
	Inh SST FRZB	64	76	
	Inh SST ADGRG6	132	31	
	Inh SST CALB1	279	64	
	Inh SST STK32A	93	17	
	Inh SST GXYLT2	41	6	
	Inh SST NPM1P10	79	8	
	Inh SST KLHDC8A	63	12	1
	Inh SST B3GAT2	182	0	
	Inh SST HPGD	60	11	
	Inh SST NPY	15	2	
VIP	Inh VIP OPRM1	52	5	
	Inh VIP SPAG17	33	6	2
	Inh VIP CASC6	45	15	1
	Inh VIP LBH	47	5	1
	Inh VIP GGH	68	4	
	Inh VIP CCDC184	64	14	1
	Inh VIP CBLN1	67	1	
	Inh VIP CHRM2	175	4	2
	Inh VIP TYR	62	1	
	Inh VIP SERPINF1	55	3	1
	Inh VIP PCDH20	61	6	2
	Inh VIP HS3ST3A1	80	5	
	Inh VIP QPCT	37	1	
	Inh VIP PENK	17	2	1
	Inh VIP ADAMTSL1	72	10	1
	Inh VIP CHRNA6	25	6	
	Inh VIP TSPAN12	42	6	
	Inh PAX6 SYT6	29	18	6
	Inh SST BAGE2	108	3	
	Inh GAD1 MC4R	107	4	
	Inh SST CHRNA4	52	0	
LAMP5	Inh LAMP5 CA1	256	42	
	Inh LAMP5 DBP	21	1	
	Inh LAMP5 LCP2	356	25	
	Inh SST NMBR	283	3	
	Inh PAX6 TNFAIP8L3	16	3	
	Inh PAX6 CDH12	90	11	

Sup. Figure 2